Journal of Materials Chemistry B

ROYAL SOCIETY OF CHEMISTRY

PAPER

View Article Online
View Journal | View Issue

Cite this: J. Mater. Chem. B, 2025, 13, 7293

A dynamically crosslinked, self-adapting, injectable gelatin–chondroitin sulfate hydrogel with antibacterial and antioxidant properties for treatment of deep and irregular wounds†

Aniruddha Dan,‡[a] Devanshi Sharma,‡[b] Hemant Singh,‡[acd] Sunny Kumar,[b] Zeel Bhatia,[b] Shabir Hassan,[cd] Sriram Seshadri *[b] and Mukesh Dhanka *[a]

Chronic, deep, and irregularly shaped wounds often infected with bacteria are considered a major clinical concern. The overproduction of reactive oxygen species (ROS) and disruption of the balance between pro-inflammatory and anti-inflammatory cytokines delay the healing process. Traditionally used dressings are unable to address these multiple issues. We present a multifunctional, self-adaptable, injectable hydrogel composed of gelatin (G) and chondroitin sulfate (CS) containing borate-crosslinked tannic acid (TA), enriched with *in situ* synthesized silver nanoparticles (AgNPs), which eliminates the necessity of any secondary dressing. The dynamically crosslinked hydrogel demonstrates efficient self-healing, adhesiveness, antioxidant properties, and potential antibacterial activity (*E. coli* and *S. aureus*). The injectable hydrogels also exhibit sustained release of TA and AgNPs. The *in vitro* cytotoxicity reveals the excellent cytocompatibility of the hydrogel with HDF-N fibroblast cells and red blood cells. *In vivo* studies confirm that the injectable hydrogel demonstrates self-adaptability in irregularly shaped wounds and accelerates the healing process in terms of healing percentage, fibroblast generation, neovascularization, and hair follicle development. Additionally, the *in vivo* application of the fabricated hydrogels does not produce any significant systemic toxicity. This study demonstrates that the dynamically crosslinked, multifunctional, injectable hydrogel is a promising candidate for treating irregular deep penetrating wounds.

Received 12th November 2024,
Accepted 10th April 2025

DOI: 10.1039/d4tb02537g

rsc.li/materials-b

Introduction

Irregular deep wounds refer to wounds with an irregular shape or configuration that penetrate the underlying tissues.[1–3] Irregular-shaped deep penetrating wounds are mainly caused by traumatic events, such as accidents (falls, cuts, or punctures), surgical procedures (like tumor resections, exploratory surgeries, or procedures involving multiple incisions), irregular-shaped deep penetrating burns, chronic wounds (pressure ulcers or diabetic foot ulcers), abscesses, or deep tissue invaded infections.[2–4] The effective management of these deep and irregularly shaped skin wounds is a noticeable major clinical concern, specifically when healing is halted by bacterial infections (*E. coli and S. aureus*), excessive oxidative stress (H_2O_2 and $^{\bullet}O_2^-$), and inflammation. However, conventional dressings are widely used to promote the wound healing process, but they are not designed to completely cover and enhance the healing of such irregular, deep wounds. The application process of traditional dressings to cover deep penetrating or irregularly shaped wounds can pose several significant challenges, including conformity to wound shape, the difficult application process, inadequate covering, maintaining moisture balance, retention, and stability, accessibility for monitoring and dressing changes, oxidative stress at the wound site, contamination and high infection risk leading to delayed wound healing.[5–7] To combat bacterial infections and excessive oxidative stress and simultaneously improve the wound's microenvironment, several materials have been explored, including the topical application of silver nanoparticles, antioxidants (curcumin), and hydrogels.[6,8,9] However, it was observed that a significant challenge in chronic wounds was to address the multiple underlying issues simultaneously to promote quick healing. However, unprecedented research in the area of hydrogel-based wound dressings has remarkably augmented their functionality and intricacy to

[a] Department of Biological Sciences and Engineering, Indian Institute of Technology Gandhinagar, Gujarat, India. E-mail: mukesh.d@iitgn.ac.in
[b] Institute of Science, Nirma University, Ahmedabad, Gujarat, India. E-mail: Sriram.seshadri@nirmauni.ac.in
[c] Department of Biological Sciences, Khalifa University of Science and Technology, Abu Dhabi, United Arab Emirates
[d] Center for Biotechnology, Khalifa University of Science and Technology, Abu Dhabi, United Arab Emirates

† Electronic supplementary information (ESI) available. See DOI: https://doi.org/10.1039/d4tb02537g

‡ These authors contributed equally.

fulfill the multiple objectives and allow remarkable control over the wound microenvironment. Engineering biomaterial-based dressings to address the challenges posed by irregular-shaped deep penetrating wounds and expedite the healing process has been emphasized.[8,10] Consequently, various biomaterials and their combinations have been utilized in formulating treatments for wound healing applications.[6,7,9,11,12] However, the therapeutic outcomes for the developed wound dressings are inadequate when it comes to irregular deep wounds.

Moreover, advanced hydrogel-based wound dressings have to be designed for chronic and irregularly shaped wounds to address multiple objectives ranging from easy application (injectability, adhesiveness, and adaptability) to promoting the overall wound healing process (antibacterial, antioxidant, maintaining moisture, and sustained delivery).[12,13] Among the biopolymers used for designing wound dressings, gelatin (G) is a highly preferred one, which is derived from collagen through partial acid or alkali hydrolysis.[14] Gelatin has been used extensively in tissue engineering due to its innate biodegradability, biocompatibility, non-immunogenicity, bio-mimicking, and other attributes.[15,16] RGD motifs make it suitable for cell attachment.[17] Gelatin is comprised of several ionizable functional groups, including the ε-amino group of lysine, guanidinium group of arginine, imidazolium group of histidine, and carboxyl groups of aspartic acid along with the terminal α-carboxyl and α-amino groups, due to which it can form polyionic complexes with other charged biomolecules including growth factors, polypeptides, and polysaccharides; also, it can be functionalized or modified according to the needs of a specific biomedical application. These complexes facilitate the controlled delivery of various biomolecules, enhancing stability and bioavailability while protecting against deterioration.[18,19] Consequently, gelatin-based formulations have been developed for wound healing, tissue engineering, anti-cancer therapies, and theragnostic applications.[20–23]

Chondroitin sulfate (CS) is a major and necessary component of the extracellular matrix in the skin tissue structure.[24,25] It is a homopolymeric unbranched glycosaminoglycan comprised of D-glucuronic acid (GlcA) and *N*-acetyl-D-galactosamine (GalNAc) residues linked through glycosidic linkages, with varying levels of sulfation.[26–28] Chondroitin sulfate is abundant and can be extracted from various biological resources.[29,30] CS plays critical roles in biological processes such as inflammation, cell proliferation, migration, differentiation, tissue morphogenesis, organogenesis, and wound healing. Moreover, it can regulate several biochemical processes, promoting fibroblast growth factor expression and increasing collagen synthesis at the wound site while suppressing inflammatory factors.[31–35] These activities are vital and ongoing throughout the healing process, particularly in the context of wound healing.[36] CS has been shown to interact with various growth factors, chemokines, and lipoproteins, thus controlling the cascade of wound closure. Additionally, CS is a flexible biopolymer that can be modified by grafting specific side groups onto it or complexing it with other bioactive polymers.[37–40]

Tannic acid (TA), a naturally occurring hydrolyzable tannin,[41] comprised of a hydrophilic shell (five digalloyl esters) surrounding a hydrophobic core (central glucose molecule), has been shown to have remarkable antioxidant and antibacterial properties.[42–44] It also acts as a vasoconstrictor and anti-inflammatory agent.[45–47] The use of TA has also been associated with the important characteristics of adhesiveness and self-healing.[48,49] Recently, there has been renewed interest in incorporating TA into sophisticated materials for advanced bio-applications. The complex chemical structure of TA, which includes several aromatic rings and hydroxyl groups, necessitates various reaction steps during the modification process.[50]

Silver nanoparticles (AgNPs) are well known for their effectiveness in wound healing due to their several beneficial properties like effective antimicrobial activity, anti-inflammatory, angiogenesis stimulation, and reduced scar formation, leading to effective wound closure and ultimately expediting the wound healing process. There are several reports regarding the fabrication of AgNP-added hydrogels for biomedical applications.[51] However, there are several disadvantages regarding the loading of externally synthesized AgNPs, such as agglomeration of silver nanoparticles, which can reduce their efficacy and may also raise toxicity issues.[52]

This study mainly focused on designing a dynamically crosslinked, multifunctional, injectable hydrogel composed of gelatin and chondroitin sulfate, along with *in situ* hybridized silver nanoparticles and borate-ester crosslinked tannic acid, for treating irregular-shaped deep penetrating wounds. To the best of our knowledge, there is no report regarding the simultaneous synthesis of silver nanoparticles along with the formation of borate ester crosslinked tannic acid in a single one-pot reaction. The present wound dressing design utilizes the microporous and extracellular matrix mimicking features of the hydrogel, along with the potential antioxidative and antibacterial properties of tannic acid (TA) and silver nanoparticles (AgNPs), respectively. Adding TA and *in situ* synthesis of AgNPs within the hydrogel facilitates dynamic crosslinking (physical and chemical crosslinking) within the hydrogel matrix, making it stable, safe, and convenient to use. A detailed optimization of the *in situ* synthesis of AgNPs, followed by their physicochemical and biological characterization, including *in vivo* mouse model studies for irregular deep penetrating wounds without using a secondary wound dressing, has been presented.

Materials and methods

Materials

Chondroitin sulfate, silver nitrate ($AgNO_3$), sodium borohydride ($NaBH_4$), dimethyl sulfoxide (DMSO), and Triton-X-100 were purchased from Sigma Aldrich. Gelatin and tannic acid were procured from LOBA Chemie, India. Collagenase, 2,2-diphenyl-1-picrylhydrazyl (DPPH), and streptomycin sulfate were obtained from TCI Chemicals, India. Ethanol and methanol were purchased from Finar, India. Mueller–Hinton agar, Mueller–Hinton broth, and Phosphate buffer saline (PBS) were purchased from HiMedia, India. Fetal bovine serum (FBS), trypsin–EDTA, MTT (3-[4,5-dimethylthiazol-2-yl]-2,5-diphenyl tetrazolium bromide), and DMEM F-12 (Dulbecco's modified Eagle's medium/Nutrient Mixture F-12) medium were procured

from Thermo Fisher Scientific, USA. *Escherichia coli* (*E. coli*) NCIM 2931 strain and *Staphylococcus aureus* (*S. aureus*) MTCC 3160 strain were procured from NCCS Pune, India. Local anesthesia (USC-Prilox cream), surgical blade, hair removal cream, and betadine were purchased from local vendors in Gandhinagar, Gujarat, India. Double-distilled and deionized water was prepared in the laboratory.

Fabrication of injectable nanocomposite hydrogels

In situ synthesized AgNP-containing gelatin/chondroitin sulphate/tannic acid nanocomposite hydrogels were fabricated. Briefly, 8.5% (w/v) gelatin and 1.5% (w/v) chondroitin sulfate were dissolved in distilled water at 60 °C in a beaker under constant stirring until a homogeneous transparent solution was obtained. Simultaneously, a desired concentration of tannic acid (TA) aqueous solution was prepared, in which $NaBH_4$ solution was added. The TA and $NaBH_4$ solution was then slowly added dropwise to the gelatin/chondroitin sulfate (G/CS) solution while stirring continuously. Subsequently, the G/CS/TA/$NaBH_4$ solution was left undisturbed for 2.5 hours to allow gel formation through potential interactions among the different components of the hydrogel. To prepare the AgNP-loaded hydrogel, all the steps were followed identically as previously mentioned, except adding a desired concentration of $AgNO_3$ solution to the TA solution, followed by the addition of $NaBH_4$ solution.

The G/CS hydrogels containing 0.5% (w/v) TA and 100 mmol L^{-1} $NaBH_4$, and 0.75% (w/v) TA and 150 mmol L^{-1} $NaBH_4$ were designated as G/CS/TA-1 and G/CS/TA-2, respectively. Similarly, G/CS hydrogels with 0.5% (w/v) TA, 100 mmol L^{-1} $NaBH_4$, and 6 mmol L^{-1} $AgNO_3$ and 0.75% (w/v) TA, 150 mmol L^{-1} $NaBH_4$, and 10 mmol L^{-1} $AgNO_3$ were referred to as G/CS/TA/AgNP-1 and G/CS/TA/AgNP-2, respectively.

Characterization of the fabricated hydrogels

Chemical characterization. The chemical characteristics (functional groups and possible interaction) of the *in situ* synthesized AgNPs and lyophilized hydrogels were investigated by Fourier transform infrared (FTIR) spectroscopy in the range of 4000 cm^{-1} to 500 cm^{-1} at a resolution of 2 cm^{-1} per point at room temperature using the PerkinElmer spectrum-2-instrument.

Furthermore, energy-dispersive X-ray (EDX) analysis was carried out to perform elemental analysis. Moreover, the X-ray diffraction (XRD) patterns of *in situ* synthesized AgNPs and fabricated hydrogel systems were determined using an X-ray diffractometer (XRD; Bruker, D8 Advance, Coventry, UK) with a diffraction angle (2θ) from 5° to 80°. The XRD graph also shows the effect of AgNPs on fabricated hydrogel systems.

The samples were characterized using UV-visible spectrophotometry (*GENESYS*, Thermo Fisher Scientific) to confirm the *in situ* synthesis of AgNPs in the hydrogel system. In brief, to produce the UV spectra of *in situ* synthesized AgNPs, the solution was first washed with deionized water through centrifugation (2040RCF, 5 min). The pellet containing AgNPs was redispersed in H_2O and analyzed using UV-spectroscopy at a 200–800 nm wavelength, keeping deionized water as the control.

Morphological analysis

The gross appearance of the fabricated hydrogels was obtained by using a digital camera immediately after the *in situ* synthesis of AgNPs and polymerization of the hydrogel system. The reduction of silver nitrate salt to AgNPs in the fabricated hydrogel was also monitored by naked-eye observation to determine if any visible change in appearance or color was going to happen, indicating the formation of silver nanoparticles.

Furthermore, the morphology of the *in situ* synthesized AgNPs and prepared hydrogels was visualized by field emission scanning electron microscopy (FE-SEM) (JEOL-JSM-7600F, magnification: 500–300 000). Initially, lyophilized hydrogels were cut, placed onto a mica sheet, and coated with gold. A high-energy electron beam is aimed at the sample to generate a topographical image. Similarly, to determine the shape, surface morphology, and size of AgNPs using FE-SEM, AgNPs were diluted and drop-casted on a glass slide, which was left inside the desiccator for drying. The drop cast sample was coated with gold under vacuum conditions, and then a high-energy electron beam was focused on the sample to capture the FE-SEM image. Later, the *in situ* synthesized AgNPs were investigated using atomic force microscopy (AFM), generating images that provided information on size, morphology, and surface texture.

Furthermore, the obtained FE-SEM images of the fabricated hydrogels were processed using ImageJ 1.40 g software from the National Institutes of Health to check the average pore size of the fabricated hydrogel. At least 20 pores were considered in this study to determine the available pore size of the hydrogel.

Porosity is defined as the percentage of void space and is a morphological property of the material. Herein, the liquid displacement method was used to evaluate the porosity (P) of the fabricated hydrogels, as explained by Purohit *et al.*[53] Briefly, the lyophilized hydrogels were placed in a measuring cylinder filled with a definite volume of ethanol (V_1). The total volume was recorded after the sample was placed in the cylinder (V_2). The samples were removed with the volume V_T, wherein ethanol was filled in the sample's pores, and the residual volume of ethanol in the measuring cylinder was denoted as V_3. The total volume (V_T) of the samples was calculated by using eqn (1).

$$V_T = V_2 - V_3 \quad (1)$$

The porosity (%) of the samples was calculated using eqn (2)

$$P\,(\%) = V_1 - V_3/V_T \times 100 \quad (2)$$

Swelling behavior

The swelling behavior study can be used to identify the hydrophilic capability of any material. This will also determine the effects of certain materials (nanomaterials) on another material's hydrophilicity. Therefore, the swelling behavior in percentage (S%) of all fabricated hydrogels was calculated using the same procedure described in prior research[54] using eqn (3).

$$S\,(\%) = \frac{W_S - W_d}{W_d} \times 100 \quad (3)$$

S% was calculated by comparing the dry samples' W_d weights with the wet sample's W_s after swelling. For this purpose, the dried samples (n = 5) were submerged in a 37 °C PBS solution. After a certain time, the samples were weighed until the swelling reached equilibrium.

Biodegradation behavior

Using the ASTM standard F-1635-95, the hydrogels' biodegradation rates were assessed under *in vitro* conditions, as mentioned in the previous literature.[55] Briefly, 1 gram of each sample (n = 5) was added to 30 mL of PBS solution. The samples were placed in a shaker incubator at 37 °C to evaluate the degradation profile and periodically withdrawn from the degradation solutions, and then the samples were wiped with tissue paper to remove any extra water droplets from the surface of hydrogel.

$$\text{Degradation } (\%) = \frac{W_0 - W_t}{W_0} \times 100 \quad (4)$$

The percentage of the degradation rate was calculated using eqn (4), where W_0 is the initial sample weight and W_t is the weight of the degraded samples at predefined time intervals.

Rheological behavior

The rheological behavior of the fabricated hydrogels was monitored by using the rheometer Anton Paar-Physica MCR 301 at 37 °C to obtain information about the loss modulus and storage modulus of the hydrogels, as mentioned in a previous report.[56] In brief, a frequency sweep was performed from 0.1 to 100 rad s^{-1}, keeping the strain fixed at 1%. Furthermore, at a constant frequency of 1 rad s^{-1}, strain sweep analysis was conducted for 0.1 to 100% strain.

Adhesiveness

Also, the adhesiveness was checked by applying the predefined amount of hydrogel to different surfaces, including glass, metal, rubber, goat skin, goat liver, goat bone, and a surgically created wound on the dorsal side of the live mouse model, and subsequently the images of the wounds containing the hydrogels were captured. Furthermore, the adhesive strength of fabricated hydrogels was tested on goat skin surfaces through the lap-shear test. Fresh goat skin was chosen as a substrate for the lap shear test. The goat skin was cut into a rectangular shape (15 mm × 40 mm) before washing with 1 M sodium hydroxide 3 times and rinsed in deionized water to remove adipose tissue. Then, rectangular-shaped hydrogels (1.5 cm × 1.5 cm) were applied to the surface of goat skin. The lap-shear test was performed on the 103B-TS electromechanical universal testing machine. The adhesion strengths of fabricated hydrogels were measured at a cross-head speed of 10 mm min^{-1}. The experiment was repeated 3 times for each hydrogel formulation.

Mechanical characterization

The mechanical properties of the fabricated hydrogels were determined using the Universal Testing System (UTS) (Instron 3365 dual column) instrument by performing compression tests. In brief, the hydrogel samples (n = 5) of definite dimensions (height: 15 mm and diameter: 16 mm) were placed over a circular plate of 70 mm diameter and allowed to compress up to 80% from the top by another circular parallel plate attached at a rate of 5 mm per minute. The stress–strain curve obtained was plotted.

Self-healing

The self-healing ability of the fabricated hydrogels was determined macroscopically by staining them with methylene blue (MB) dye. In this technique, one piece was stained with MB dye, and another piece of hydrogel was kept unstained. Then, both pieces of hydrogel with different colors were placed together at room temperature for 60 min to allow them to merge into a single hydrogel unit again. Then, photographs of this self-healed hydrogel were captured, and the healing ability was observed. Also, the self-healing ability of the fabricated hydrogels was determined by performing step-strain analysis from 0.1% to 10% strain, and the variation in the modulus was recorded. Each experiment was repeated 3 times.

Syringeability

A syringeability test was performed using the reference method reported by Moreira *et al.*[57] with necessary modifications. This test used a syringe of 2 mL with an inner diameter of 1.5 cm and a 24 G needle. The weight of the hydrogel before and after injection within 2 minutes was measured, and its syringeability was calculated using the following equation (eqn (5)). The injectability and shear thinning properties of the fabricated hydrogels were determined through a shear-dependent change in the viscosity of the fabricated hydrogel in the step-shear test with alternating low shear (0.1 s^{-1}) to high shear (100 s^{-1}).

$$\text{Syringeability } (\%) = \frac{\text{Mass expelled from the syringe}}{\text{Mass of the sample prior to injection}} \times 100 \quad (5)$$

Release behavior analysis

A dialysis approach was used to assess the release behavior of several samples, as described in previous reports.[19,56] A particular quantity of each sample (n = 3) was put into a dialysis membrane and incubated for 96 hours at 37 °C with continual stirring at 60 RPM in 20 mL of PBS (pH 7.4). 5 mL of the release media was collected, and new PBS was added at regular intervals. The collected solution was examined using a UV spectrophotometer (Shimadzu UV 1800) at wavelengths of 280 nm and 425 nm for TA and AgNPs, respectively. The following equation (eqn (6)) was used to calculate the amount of curcumin released in the sample that was collected.

$$\text{Cummulative release } (\%) = \frac{\text{Released amount of therapeutics}}{\text{Initially loaded amount of therapeutics}} \times 100 \quad (6)$$

Furthermore, to determine the mechanism of the release of therapeutics, *i.e.* here TA and AgNPs from the hydrogel, we have assessed the release data of each of the hydrogel through

several kinetic models (Table S1, ESI†) (zero-order, first-order, Higuchi, Hixson–Crowell, and Korsmeyer–Peppas)[54] and the best-fitted model was selected, through which it was predicted that either diffusion or dissolution/erosion of the matrix, *etc.* is involved in the release.

In vitro antioxidant assay

Based on a previous study,[58] the DPPH test was carried out to assess the samples' antioxidant activity, particularly their capacity to scavenge free radicals. In brief, all different compositions of hydrogels were incubated with PBS (pH 7.4). 12 h later, the PBS containing the released substances was collected. The suspension of each sample ($n = 5$) was exposed to DPPH (100 μM) in methanol in a dark environment. Using a spectrophotometer, the absorbance of the solutions was determined at 517 nm at pre-defined time intervals. Methanol and DPPH were used in equal quantities to prepare the blank and negative control. Eqn (7) was used to calculate the percentage of scavenged free radicals to determine the antioxidant activity.

$$\text{Antioxidant activity } (\%) = \frac{\text{Abs of DPPH} - \text{Abs of sample treated DPPH}}{\text{Abs of DPPH}} \times 100 \quad (7)$$

Biological characterization

Hemocompatibility assay. A method reported by Dave *et al.*[59] was used to assess the *in vitro* blood cell compatibility of the fabricated hydrogels. In this procedure, 1 mL of blood was drawn into an anticoagulant tube from a healthy Balb/c mouse. Then, the blood was centrifuged at 1500 rpm for 5 minutes to collect the RBCs. The supernatant was discarded, and the pellet containing RBCs was diluted with PBS (pH 7.2) in a volumetric ratio of 1 : 9 (RBC : PBS). After that, each of the hydrogel samples ($n = 5$) was submerged in 5 mL of diluted blood and incubated for 4 hours at 37 °C. The samples were centrifuged at 1500 rpm for 10 minutes, and a UV-visible spectrophotometer was used to determine the supernatant's optical density (OD) at 540 nm. PBS and Triton-X were used as the negative and positive controls, respectively. Eqn (8) below shows how to use the OD measurements to calculate the percentage of hemolysis.

$$\text{Hemolysis } (\%) = \left(\frac{\text{OD of sample} - \text{OD of negative control}}{\text{OD of positive control} - \text{OD of negative control}}\right) \times 100 \quad (8)$$

In vitro cytotoxicity assay

In vitro biocompatibility of the fabricated injectable hydrogels was verified by MTT assay, according to a previous report.[19] The experiment used human dermal fibroblasts-neonatal (HDF-n) cells for evaluating *in vitro* cytotoxicity. For this purpose, sterilized hydrogels in a certain amount in triplicate were added to the tissue culture plate (TCP) and loaded with DMEM medium (10% FBS and 1% antibiotic/antimycotic). Then, the HDF-n cells were seeded over the hydrogel, and PBS was used as the control under sterile conditions and allowed to incubate in a mammalian cell-culture-grade CO_2 incubator at 37 °C. After 24 hours and 72 hours, the DMEM medium was removed and washed with PBS solution. Then, the MTT dye (50 μL of 5 mg mL^{-1} in PBS) was added to each well under dark conditions and left for four hours in the incubator. After that, aliquots were pipetted out, and a solubilization buffer was added to dissolve the formazan crystals. The microplate reader measured the absorbance of each well at 570 nm to assess the cell proliferation and cell viability, which was determined using eqn (9). Furthermore, to visualize and quantify the live/dead cells, follow the same protocol as mentioned for the MTT assay, except for replacing the MTT assay with live/dead assay. Then, live and dead cell pictures were taken using a fluorescence microscope.

$$\text{Cell viability } (\%) = \frac{\text{Abs of treatment}}{\text{Abs of control}} \times 100 \quad (9)$$

In vitro antibacterial assay

A typical approach for assessing a material's antibacterial activity is the turbidity measurement method.[54] The bacterial solution is standardized in this approach between 0.1 and 0.2 absorbance values (equal to 0.5 McFarland standard) at 625 nm before the bacterial strains are cultured in Mueller–Hinton broth solution. This standardization is crucial because it confirms that the concentration of bacteria is the same in all samples, enabling precise comparisons.

The standardized bacterial solution is then added to each sample ($n = 5$) to be tested, and the mixture is incubated in an incubator with gentle shaking at 37 °C. Using a spectrophotometer set to 625 nm, the solutions' OD values are measured after 24 hours of incubation. The OD values show how much bacterial growth is present in the sample. Lower OD readings result from the material's ability to suppress bacterial growth if it possesses antibacterial qualities. Antibacterial activity was analyzed using eqn (10)

$$\text{Bi } (\%) = \frac{A_c - A_s}{A_c} \times 100 \quad (10)$$

Bi(%) stands for bacterial inhibition (%), A_c and A_s are the OD values of the bacterial solution without and bacterial solution with samples, respectively.

Another approach, the diffusion method, was employed to evaluate the antibacterial activity of the fabricated hydrogels. The procedure was followed as mentioned in previous reports.[19,56] In brief, sterile Mueller–Hinton agar was added to sterile Petri plates, and the plates were left undisturbed to solidify. Once the agar was properly solidified, 100 μL of standardized bacterial solutions (*E. coli* and *S. aureus*) were spread uniformly throughout the Petri plates separately. Further wells with certain dimensions (diameter: 5 mm and depth: 5 mm) were made inside the solidified agar, where freshly prepared sterile hydrogels ($n = 5$) were injected. PBS and streptomycin solutions were taken as negative and positive controls, respectively. Plates were incubated for 24 hours at 37 °C, and then the clear inhibition zone surrounding each well was measured.

In vivo assessment

To assess the feasibility and applicability of the fabricated hydrogels, an irregular full-thickness wound model was created using Balb/c mice. Briefly, a total number of 12 Balb/c mice (25–35 g) were utilized for the wound healing experimental study. Animals were kept for one week of acclimatization at the animal house of Nirma University, Gujarat, India. The animals were kept in clean cages and maintained in a 12 : 12 h dark–light cycle at a standard room temperature of 22 °C. Food and water were adequately provided, with a sample size $n = 3$ for each group. All the animal procedures were carried out according to the ethical guidelines for the care and use of laboratory animals of the Institutional Animal Care and Use Committee, Nirma University, Ahmedabad, under the CPCSEA guidelines of the Ministry of Environment and Forest, New Delhi of the ISNU ethical committee protocol code (IS/FAC/30/2022/33). Irregular wound excisions were created according to the early proposed method,[60] wherein the animals were first locally anesthetized *via* topical application of the lignocaine gel after shaving their dorsal hair and cleaning with 70% ethanol. The open irregular wounds were made using a surgical blade, where a full-thickness cross (1 × 1 cm) was cut. The wounds were cleaned with saline, and the animals were housed individually. The animals were randomly allocated into four groups (3 mice per group). Group 1 served as a negative control, where the wounds of these animals were left without treatment. Group 2 served as a positive control, wherein commercially available betadine was applied topically to the wound. Group 3 served as the vehicle material with the formulation named G/CS/TA, and Group 4 comprised the loaded material with a formulation containing AgNPs named G/CS/TA/AgNP-2.

Progressive changes in wound healing were assessed quantitatively using Image J 1.52 software. The wound area was calculated using scaled pictures of the wounds on days 0, 3, 6, 10, and 14, and the hydrogel was applied to the wound every 72 hours (0th day, 3rd day, 6th day, and 10th day). Percentage healing was calculated using the following equation (eqn (11)), where n = the number of days (3, 6, 10, or 14) that the healed area was read.

$$\text{Healing}\ (\%) = \frac{\text{wound area (0 day)} - \text{wound area on } n\text{th day}}{\text{wound area (0 day)}} \times 100 \quad (11)$$

Furthermore, on the 14th day, the animals were sacrificed, and skin tissue samples from the healed wound area and liver tissues were preserved in 10% neutral buffered formalin for histopathological examination. The specimens were routinely processed and stained with hematoxylin and eosin (H&E). Microscopic wound healing criteria were assessed, encompassing re-epithelialization, angiogenesis, hair follicle formation, granular tissue formation, and fibroblast growth. Additionally, H&E-stained liver tissues were examined to assess the toxicity of the applied wound–healing material (injectable hydrogels). Moreover, to evaluate the anti-inflammatory efficacy of the formulations and correlate wound healing, a sandwich enzyme-linked immunosorbent assay (ELISA) was performed as per the manufacturer's instructions (ElabScience, USA) for the qunatification of TNF-α, TGF-β, IL-1α, and IL-10 present in the serum sample taken on the 14th day of the *in vivo* study.

Statistical analysis

The data were presented as mean values with standard deviation (± SD), and p-values less than 0.05 were considered statistically significant. Student's t-test and one-way analysis of variance (ANOVA) were used to determine statistical significance as appropriate. Statistical analyses were performed using Origin Pro 2024 and Microsoft Office Excel 2021. Each experiment was independently replicated at least three times to collect statistically significant data.

Results and discussion

Physico-chemical properties of fabricated hydrogels

The rationally designed, dynamically crosslinked, self-adaptable, easily injectable hydrogels composed of chondroitin sulfate and gelatin, further enriched with the natural antioxidant tannic acid and the potential antibacterial agent nano-silver, designated as G/CS/TA and G/CS/TA/AgNP hydrogels, respectively, were fabricated using $NaBH_4$ as an *in situ* crosslinking and reducing agent. Ag^+ was reduced to Ag^0 by $NaBH_4$. AgNPs containing hydrogel composites were prepared using different concentrations of $AgNO_3$ solution (6 mM and 10 mM). Gelatin and chondroitin sulfate-based *in situ* synthesized AgNP-loaded nanocomposite hydrogels were fabricated following the steps illustrated in Fig. 1. During the fabrication process, the components of the hydrogel composite system are dynamically crosslinked by involving multiple interactions, including physical and chemical bonding, as illustrated in Fig. 1. Sodium borohydride ($NaBH_4$) has a very significant effect both in the gelation of the G/CS/TA hydrogel composite and *in situ* synthesis of AgNPs by reducing Ag(I) ions to Ag(0). During the synthesis of AgNPs, partial catechol groups of tannic acid are converted into quinones, and tannic acid might be adsorbed onto the surface of synthesized AgNPs through interaction between carboxyl (═C═O) and hydroxyl (–OH) groups and AgNPs. Sodium borohydride ($NaBH_4$) rapidly dissociates into sodium metaborate ($NaBO_2$). Sodium metaborate is thermodynamically unstable, and it is readily transformed into the tetrahydroxyborate anion $B(OH_4)^-$.[61] Tannic acid is a natural polyphenol enriched with many hydroxyl groups; chondroitin sulfate also contains hydroxyl groups in its structure. So, once we added the $NaBH_4$ solution to the solution containing tannic acid and $AgNO_3$, immediately the color of the solution turned brown, confirming the rapid synthesis of silver nanoparticles, simultaneously producing the tetrahydroxy borate anions ($B(OH_4)^-$). These $B(OH_4)^-$ anions could form borate esters with two pairs of *cis*-diol groups of tannic acid (Fig. 2(A)) creating an intermolecular complex of tannic acid and also giving rise to the crosslinked 3D structure of hydrogel composite systems, as demonstrated in Fig. 1. Dynamic crosslinking can be described as any type of bond that can break and reform simultaneously or in response to any physical or chemical stimuli.

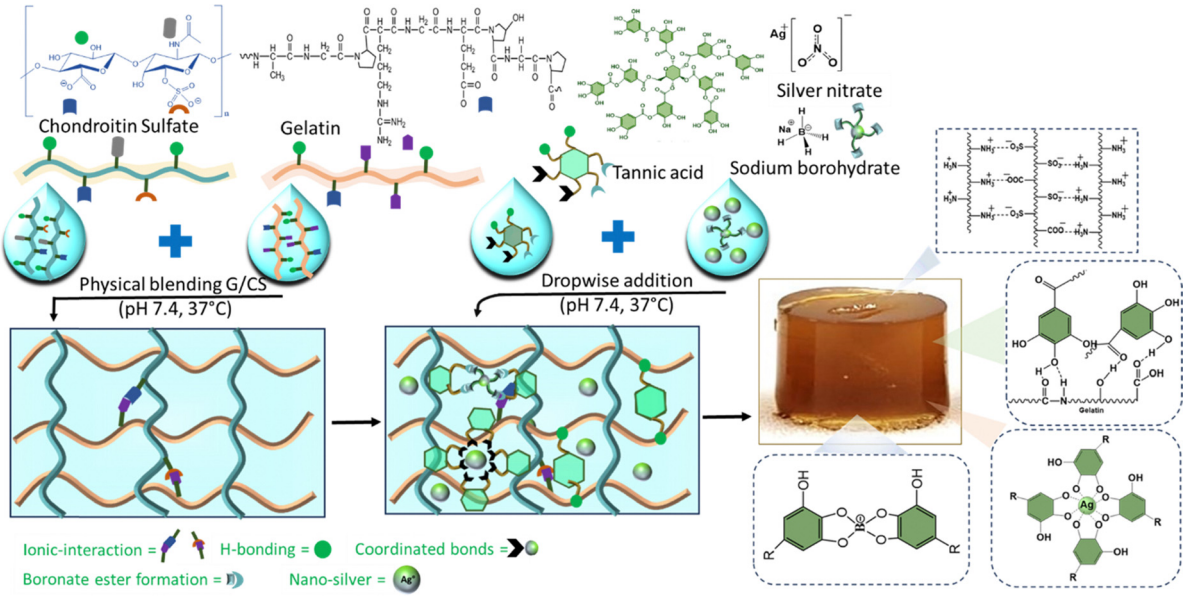

Fig. 1 Schematic illustration of the fabrication of the gelatin–chondroitin sulphate based self-adaptable tannic acid and silver nano enriched injectable hydrogel system for irregular deep penetrating wounds, along with possible interactions.

Dynamic crosslinking imparts hydrogels with adaptable characteristics like injectability and self-healing. Multiple types of physical interactions including H-bonding between tannic acid, gelatin, and chondroitin sulphate, π–π interactions between tannic acids and chemical covalent crosslinking for borate ester formation between *cis*-diol groups of tannic acid and chondroitin sulphate give rise to a dynamically crosslinked G–CS–TA hydrogel. Similar types of findings were also reported.[62,63]

FTIR spectra of G/CS/TA and G–CS–TA/AgNPs were compared to determine the presence of several important functionalities inside the hydrogel components and their contribution to different interactions, which gave rise to the crosslinked hydrogel composite. Fig. 2(B) shows a broad absorption band at 3291 cm^{-1} due to the stretching of N–H and polyphenolic OH of TA.[64] C–H stretching in aromatic rings of TA produced the band at 3066 cm^{-1}. The band at 1747 cm^{-1} denotes the oxidation of polyphenolic hydroxyls into carboxyl groups. Distinct bands due to amide I, amide II, and amide III are present at 1637 cm^{-1}, 1538 cm^{-1}, and 1233 cm^{-1}, respectively. The band at 1233 cm^{-1} also corresponds to the asymmetric extension of B–O–C, proving the intermolecular crosslinking of *cis*-diols of tannic acid by $B(OH_4)^-$ derived from $NaBH_4$.[65]

In the case of G–CS–TA/AgNP hydrogels, slight modifications can be observed, including weak intensities of the bands at 3291 cm^{-1} and 1747 cm^{-1}, which might be due to the interactions of –OH, –NH, and C═O groups with silver nanoparticles.

Fig. 2(C) shows the XRD spectra of AgNPs. The diffraction peaks at 2θ values of 45.879°, 66.547°, and 75.5893° signifying the 200, 220, and 311 planes confirm the crystalline nature of silver nanoparticles. The peaks at 32.1268°, 27.7547°, and 56.8688° might be due to unreacted $AgNO_3$. Furthermore, the XRD pattern of G–CS–TA, G–CS–TA/AgNP hydrogels depicts that the hydrogel without AgNPs does not show any peaks, signifying the loading of AgNPs in the hydrogel composite system. However, the hydrogel containing AgNPs has provided significant peaks (45.879° and 75.5893°) similar to that of silver nanoparticles, confirming the successful loading of silver nanoparticles inside the hydrogel. UV-spectra of AgNPs in Fig. 2(D) show a peak at 420 nm. A peak at 420 nm is due to the SPR (SurfacePlasmon Resonance) of synthesized nanoparticles, according to the previous reports.[63] Moreover, the DLS and zeta potential outcomes show that the AgNPs have a hydrodynamics radius of about 247.3 nm. The PDI value is 0.263, referring to the mono-dispersity of synthesized silver nanoparticles. Fig. 2(E) displays the FESEM images of synthesized AgNPs during the hydrogel fabrication process. The FESEM images of *in situ* synthesized silver nanoparticles depict that these AgNPs are monodispersed and spherical in shape and have a smooth surface. The size of synthesized silver nanoparticles was determined by using ImageJ software from SEM images. The distribution curve displayed in Fig. 2(H) shows that the average size of AgNPs is 25 nm. Also, the AFM image in Fig. 2(F) confirms the spherical nature of AgNPs. Furthermore, the production of AgNPs was initially investigated through UV-visible spectroscopy. The *in situ* synthesis of silver nanoparticles during the fabrication of the hydrogels faces the main obstacle to making these silver nanoparticles uniform in shape and size and avoiding their agglomeration so that their bioactivity doesn't get affected. Fig. 2(G) shows the EDS spectra, depicting the presence of Ag (77%), confirming the *in situ* synthesis of AgNPs; the findings were similar to previously reported research.[62] Initially, the physical appearance of the formulated hydrogel showed a uniform distribution of tannic acid and silver nanoparticles with high reproducibility with brown colour with increasing concentration of the tannic acid and silver nanoparticles, as shown in Fig. 2(I).

Furthermore, the morphology of the fabricated hydrogels was also visualized by acquiring the FESEM images of the four

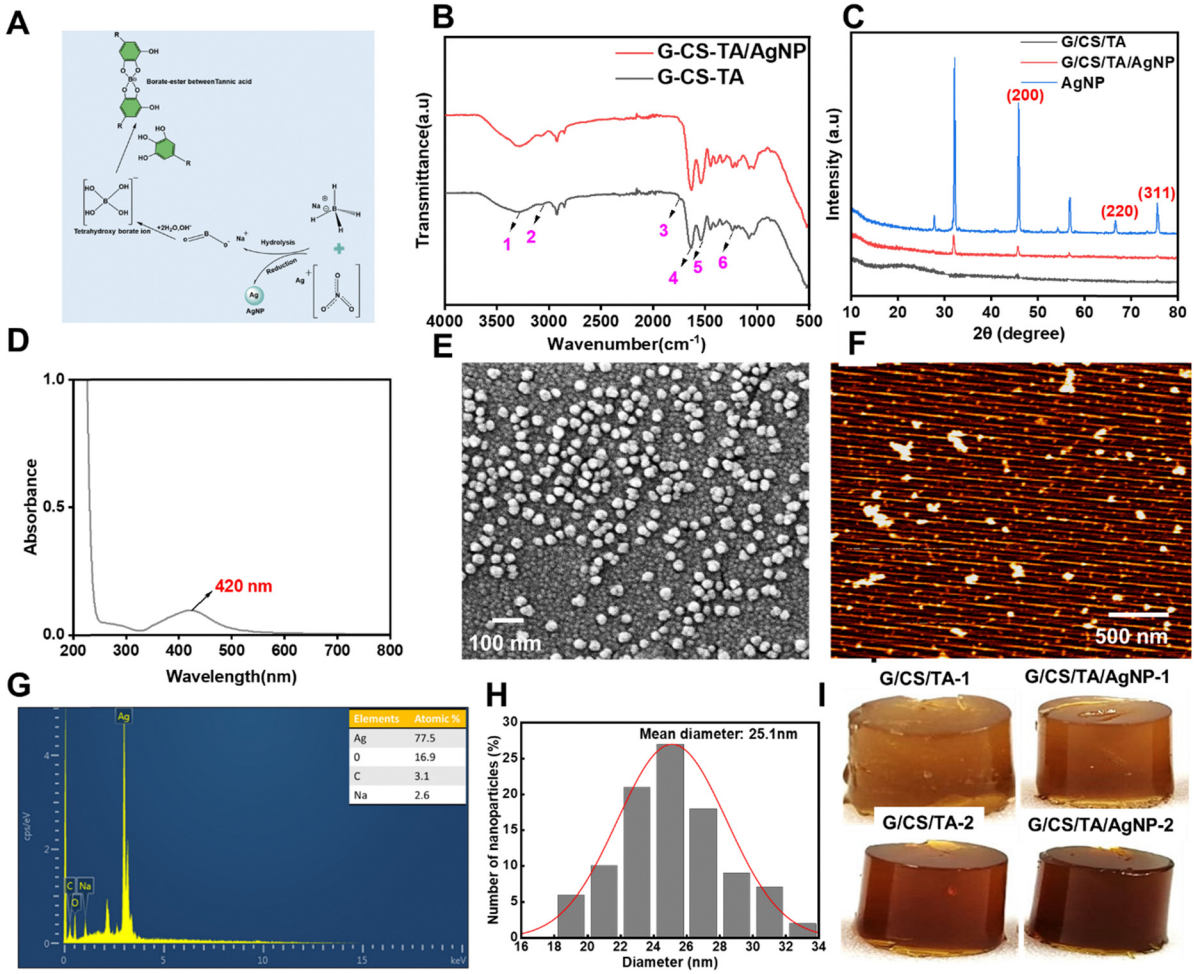

Fig. 2 (A) *In situ* synthesis mechanism of silver nanoparticles. (B) FTIR spectra of the hydrogels. (C) XRD spectra of hydrogels and synthesized silver nanoparticles. (D) UV-spectra of the synthesized silver nanoparticles. (E) Morphology (FESEM images) of synthesized silver nanoparticles. (F) AFM images of the synthesized silver nanoparticles. (G) EDS spectra of the synthesized silver nanoparticles. (H) Mean diameter of synthesized silver nanoparticles. (I) Macrograph of the various fabricated hydrogels showing the physical appearance and stability.

different compositions of hydrogels, which shows the porous structure of scaffolds, Fig. 3(A). The presence of inter-connected pores makes them competent for retaining large amounts of wound exudate; most necessarily, various types of cells of skin layers can grow and communicate and exchange nutrients between them inside the hydrogel, which might give rise to the new healthy skin layers. Moreover, using the Image J software, the pore size was calculated, which was around 163 μm, as shown in Fig. 3(B). It can be observed that the pore size has not varied remarkably, with the varying concentrations of tannic acid and AgNPs. The pore size is large enough for fibroblast cells to grow, divide, and replenish their population. Furthermore, Fig. 3(C) shows the average porosity of all scaffolds, which was found to be more than 80%, and no significant difference in the porosity was observed among the scaffolds. Furthermore, to evaluate the hydrophilic nature of the scaffolds, the swelling percentage was measured, as depicted in Fig. 3(D), which demonstrated that all the scaffolds were entirely hydrated within 200 hours and all the scaffolds showed perpetual swelling. However, the swelling percentage of the scaffolds was increased with increasing concentrations of tannic acid and silver nanoparticles. Moreover, the degradation tendency was also investigated, as shown in Fig. 3(E). This indicates good biodegradability. The hydrogels containing AgNPs were degraded at a faster rate compared to the hydrogels without AgNPs, which may be due to the faster release of the TA from the hydrogels containing AgNPs in contrast to the hydrogels without AgNPs.

The dynamic rheological behavior of the fabricated hydrogels is shown in Fig. 3(F) and (G). To elucidate the viscoelastic features of the composite hydrogels, a frequency sweep was performed. As observed in Fig. 3(F), for all the hydrogel formulations, the storage modulus (G') was greater than the loss modulus (G''), which denotes the strong intermolecular interactions in hydrogels. The storage modulus (G') of all the hydrogel formulations behaves in a nearly frequency-independent manner, indicating the formation of stable crosslinked networks, ultimately giving rise to the 3D structure of the hydrogel. Also, the storage modulus (G') increased gradually with increasing concentration of TA and AgNPs, confirming the formation of a more reversible crosslinking network. Furthermore, through

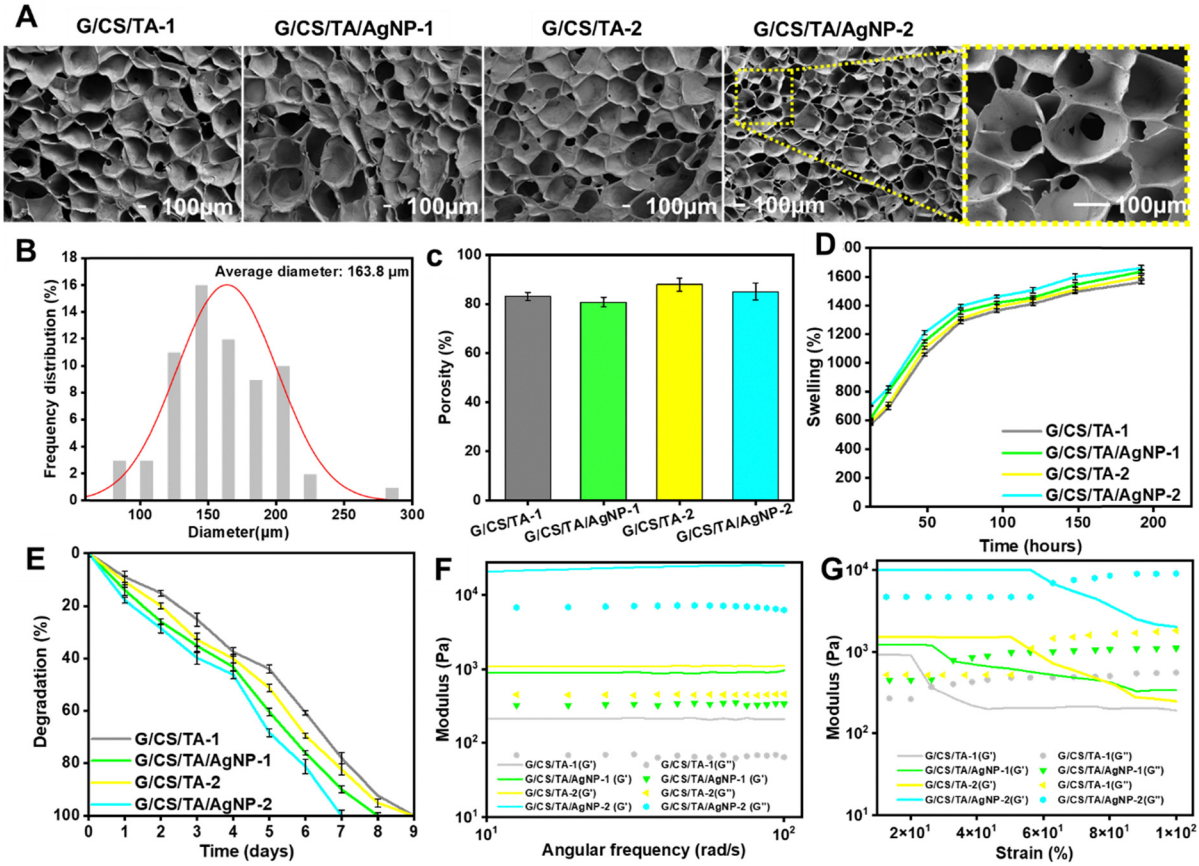

Fig. 3 (A) SEM images of G/CS/TA-1, G/CS/TA/AgNP-1, G/CS/TA-2, and G/CS/TA/AgNP-2. Zoomed-in SEM images of G/CS/TA/AgNP-2 demonstrating the interconnecting pore size good for cell growth and transportation of gases and nutrient for cells. (B) Average pore size distribution of the different fabricated hydrogels. (C) Porosity percent of the different hydrogels. (D) Comparison of swelling behaviour of fabricated hydrogels. (E) Degradation behaviour of the fabricated hydrogels. (F) Frequency sweep analysis of fabricated hydrogels. (G) Strain sweep analysis of the fabricated hydrogels.

strain sweep experiments, the linear viscoelastic region (LVER) and yielding point of the respective hydrogel formulations were determined. As shown in Fig. 3(G), with increasing strain, the G' suddenly decreases and simultaneously the G'' increases, confirming the disruption of the intermolecular network of the hydrogels. The cross-over point or the yield point appears to be at 26.5%, 50.5%, 56.9%, 62.9% of strain for G/CS/TA-1, G/CS/TA/AgNP-1, G/CS/TA-2, and G/CS/TA/AgNP-2 hydrogels. This yield point depicts the sol–gel transition of hydrogels, confirming the injectability of the fabricated hydrogels.

Adhesiveness

The adhesive properties of the hydrogels were checked by applying the hydrogel samples on different types of material surfaces, including metal, glass, rubber, goat skin, goat liver, goat bone, *etc.* As shown in Fig. 4(A) the hydrogels stick to different types of surfaces without getting detached. Even the hydrogel adhered to the wound site in mice, suggesting the real-time adhesiveness of the fabricated hydrogels. This adhesive nature might be attributed to the presence of tannic acid molecules in the hydrogels, as similar properties of tannic acid have been reported earlier (Fig. 4(B)).[66–70] Also, through the lap shear test, the quantitative analysis of the adhesive strength of the fabricated hydrogels was conducted. It can be depicted from Fig. 4(C) that the adhesive strength of G/CS/TA-1, G/CS/TA/AgNP-1, G/CS/TA-2, and G/CS/TA/AgNP-2 is 16 kPa, 32 kPa, 36 kPa, and 45 kPa respectively. The adhesive strength of the hydrogels has increased with an increase in the concentration of TA and AgNPs.

Mechanical properties

Compressive stress–strain tests were performed to determine the mechanical features of the fabricated hydrogels. Fig. 4(D) demonstrates that all the fabricated hydrogels have favorable mechanical properties to be used as wound dressings. All fabricated nano-composite hydrogels exhibited typical "J" shaped curves, confirming their tolerance against compressive stress. G/CS/TA-1 exhibited a compressive stress of 0.17397 MPa at 74% of strain. G/CS/TA-2 exhibited a compressive stress of 0.68003 MPa at 81% of strain. AgNP-loaded nano-composite hydrogels have shown better compressive stress tolerance in comparison to hydrogels without AgNPs. The compressive stress tolerance capacity of the hydrogels has increased with an increase in concentrations of both TA and AgNPs. G/CS/TA-AgNP1 and G/CS/TA-AgNP2 exhibited compressive stress values of 0.70 MPa and 0.956 MPa at a strain of 88%. The G/CS/TA-AgNP2 nano-composite hydrogel exhibited the highest compressive stress of 0.956 MPa, which is almost six

times that of G/CS/TA-1; this increase in compression stress tolerance might be due to increase in interaction due to more H-bonding formation, borate-ester formation, and metal–phenolic co-ordination along with the increase in the concentration of TA and AgNPs.

Self-healing

The self-healing nature of the hydrogels is shown in Fig. 4(E). The different colored hydrogels were kept together without any external stimulus, and after 60 minutes, the different colored hydrogels self-healed to become one single hydrogel. This self-healing property may be due to the reversible borate ester-based cross-linking along with hydrogen bonds and π–π interaction (Fig. S2, ESI†), similar to the previous reports.[62] Also, through the step-strain test, the reversible change in the modulus of the hydrogels was observed. The step-strain demonstrated that at lower strain, the storage modulus (G') was greater than the loss modulus (G''), but once the strain was increased, the storage modulus (G') dropped even below the loss modulus (G''); also, upon reducing the strain from the high strain, the storage modulus recovered as it was initially (Fig. 4(F)). Thus, this confirmed the self-healing ability of the fabricated hydrogels.

Injectability

The syringeability of the hydrogels was excellent as nearly 100% of all the hydrogel formulations extruded from the injections (TableS3, ESI†); also, the pre-gel solution can be easily loaded into a 5 mL syringe as shown in Fig. S1(A) (ESI†). Furthermore, the fabricated hydrogels were injected through an injection device equipped with a 24 G needle (Fig. S1(B), ESI†) and distinct letters were written (Fig. S1(C), ESI†) while injecting through the injection device to demonstrate both excellent injectability and printability of the fabricated hydrogels. The shear-dependent viscosity changes of all the hydrogel formulations were reversible

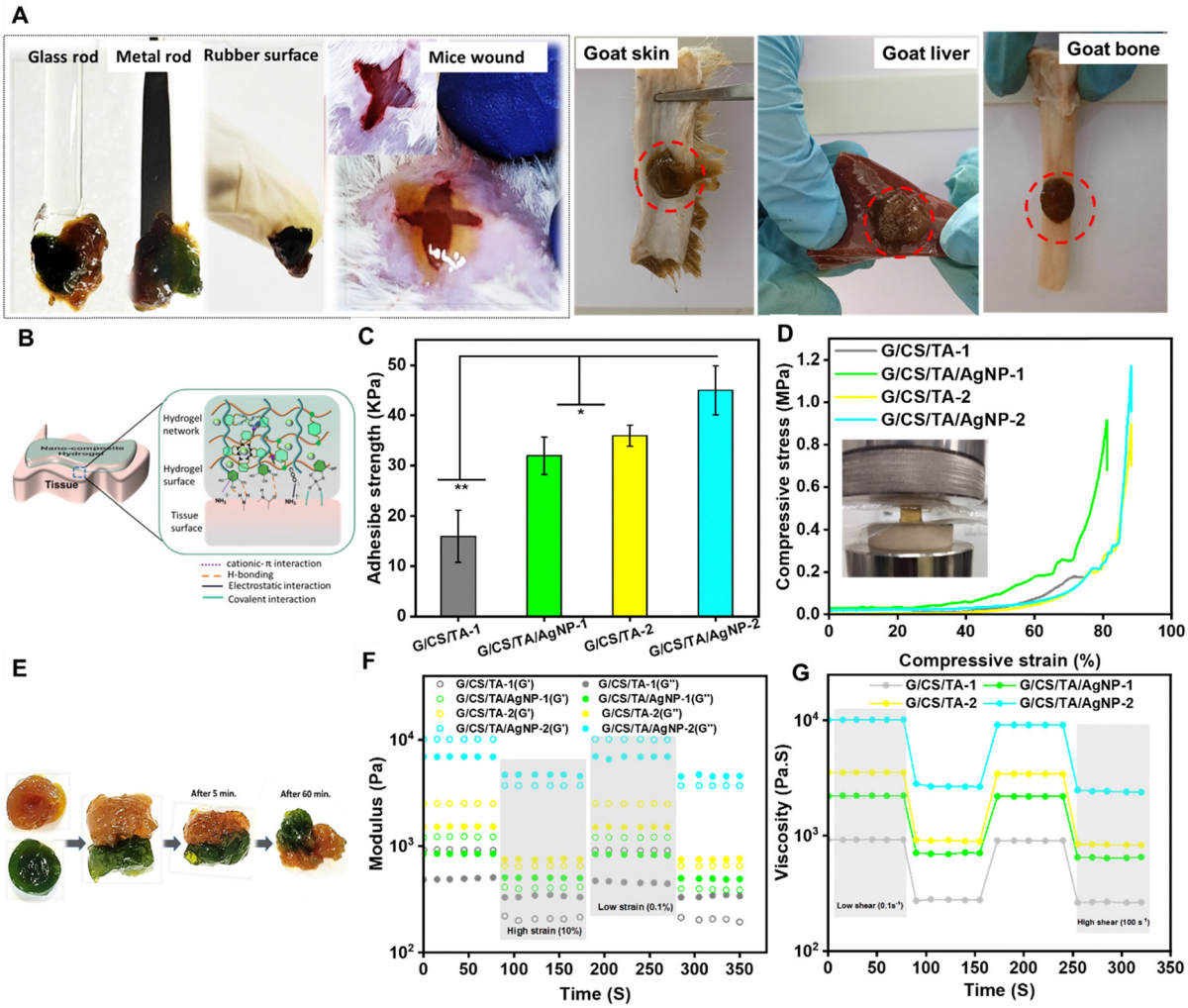

Fig. 4 (A) Adhesiveness of the fabricated hydrogels on different surfaces (glass rod, rubber, live mice wound, goat skin, goat liver, and goat bone). (B) Mechanism of hydrogel adhesion. (C) Quantitative analysis of the adhesive strength of fabricated hydrogels was determined through the lap-shear test. (D) Compressive stress–strain curve of fabricated hydrogels. (E) Visual self-healing of the fabricated hydrogel. (F) Step-strain measurements of fabricated hydrogels, alternate step-strain from low (0.1%) to high (10%) strain, with a frequency of 1 rad s^{-1}. (G) Step-shear measurements of fabricated hydrogels, with alternate shear switch from low shear (0.1 s^{-1}) rates to high shear (100 s^{-1}) rates.

when subjected to a cyclic shear switch from a low shear rate (0.1 s^{-1}) to a high shear rate (100 s^{-1}), as shown in Fig. 4(G). This indicates the shear thinning behaviour of the fabricated hydrogels, as the viscosity of the hydrogel is maintained when low shear is applied, but the viscosity reduced when a high shear rate is applied. So, the hydrogel becomes a sol inside the

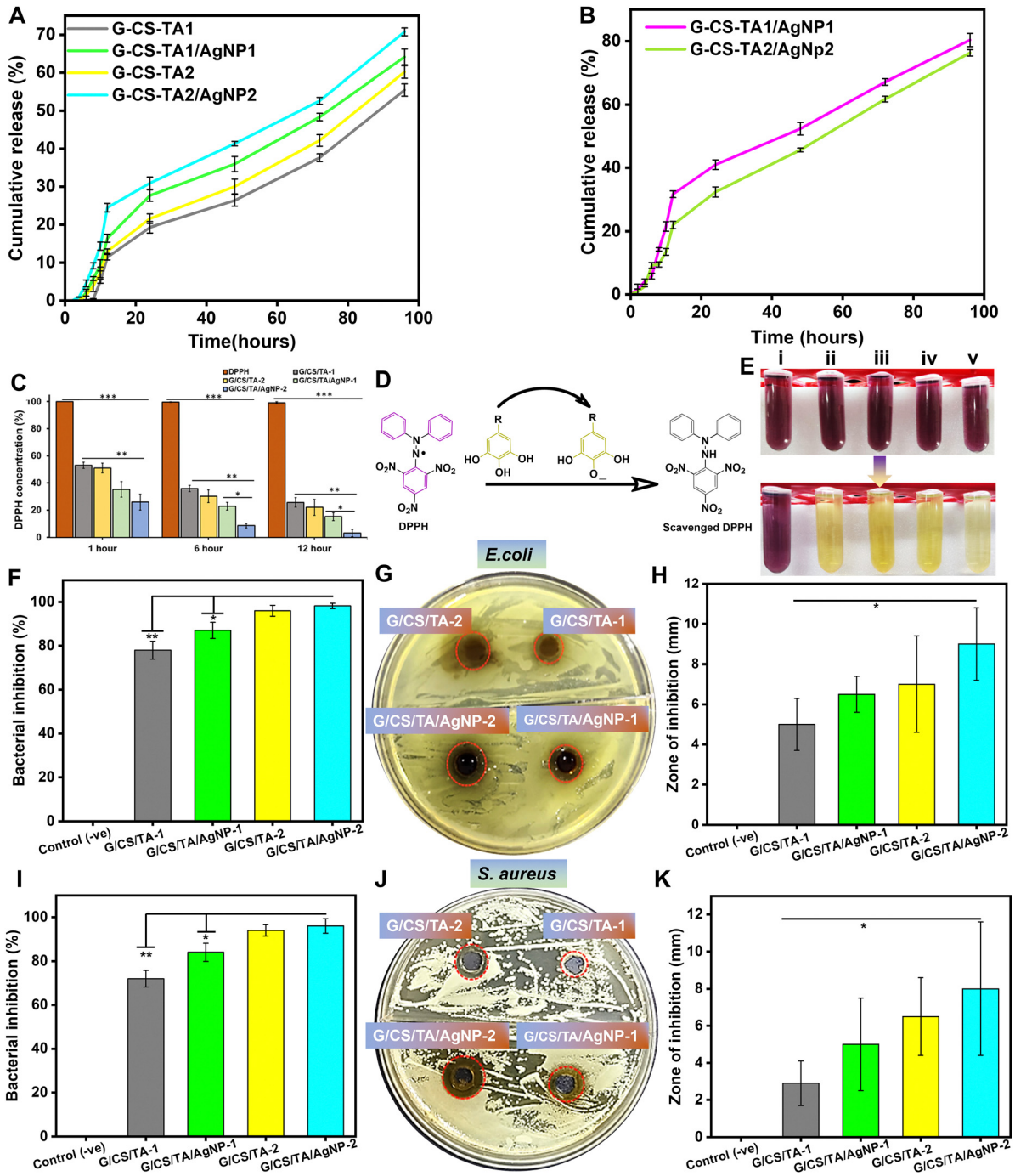

Fig. 5 (A) Cumulative release of tannic acid from different compositions of the hydrogels. (B) Cumulative release of AgNPs from different compositions of the hydrogel. (C) Quantitative analysis of the percentage of free radical scavenging activity. (D) Mechanism of free radical scavenging activity. (E) Antioxidant activity of the fabricated hydrogels, where macrographs represent the free radical scavenging activity of the hydrogels after 12 hours; (i) Untreated DPPH, (ii) G/CS/TA-1, (iii) G/CS/TA/AgNP-1, (iv) G/CS/TA-2, and (v) G/CS/TA/AgNP-2 treated DPPH respectively. (F) Quantification of the antibacterial activity in terms of the percentage of bacterial (*E. coli*) inhibition by the fabricated hydrogels *via* a turbidity method. (G) Zone of inhibition against *E. coli*. (H) Quantitative analysis of the zone of inhibition against *E. coli*. (I) Quantification of the antibacterial activity in terms of the percentage of bacterial (*S. aureus*) inhibition by the fabricated hydrogels *via* a turbidity method. (J) Zone of inhibition against *S. aureus* and (K) quantitative analysis of the zone of inhibition against *S. aureus*. Here, columns/lines and error bars represent mean and standard deviation, whereas *p <0.05, **p <0.005, and ***p <0.0005 show the statistical difference.

injection syringe, but once it is extruded outside the syringe, it becomes a gel, regaining its viscosity.

Drug release behaviour

The release profiles of TA and AgNPs are shown in Fig. 5(A) and (B), respectively, which shows that both TA and AgNPs have been sustainably released over 96 hours. In the case of G–CS–TA/AgNP hydrogels, it can be observed that silver nanoparticles have accelerated the release of tannic acid compared to the hydrogel without silver nanoparticles. Both the AgNPs and TA have been released in a biphasic manner, showing burst release up to 15 hours followed by a sustainable release for 80 hours. The initial burst release of TA molecules could be due to several aspects, including (1) the effect of surface-bound AgNPs and TA molecules, which were released due to their highly hydrophilic nature and (2) the TA molecules form many non-covalent physical interactions like hydrogen bonds with other components of the hydrogels, but at basic pH of the PBS the phenolic OH groups oxidize into quinone groups and these hydrogen bonds are disrupted, which has been also highlighted in a previous report.[71] This sustainable release of TA and AgNPs is very beneficial for extended antibacterial, anti-inflammatory, and antioxidant activities at the site of the wound.

Furthermore, the TA and AgNP release data of each hydrogel were processed in several mathematical kinetic models to check the release kinetics behavior (Fig. S3 and S4, ESI†). According to the correlation coefficient (R^2), depicted in Tables S4 and S5, ESI,† it can be observed that the release of both TA and AgNPs follows the Hixson model[72] in a better way compared to other models. R^2 values of both TA and AgNPs fitted the Hixson-model properly, and this indicates that both the therapeutics (TA and AgNPs) have been released from the porous hydrogel matrix due to the dissolution of the hydrogel matrix over the time period.[73,74]

Antioxidant activity

If reactive oxygen species (ROS) accumulate at the wound site, it causes oxidative stress/damage to the surrounding tissues, leading to delayed healing and an increased risk of infection. Therefore, fabricated hydrogels were equipped with free radical scavenging agents to neutralize or inhibit the harmful effects of reactive molecules/free radicals. The free radical scavenging capability of fabricated hydrogels is visualized in Fig. 5(C) after 12 hours through the DPPH scavenging assay. Increasing the concentration of the tannic acid and silver nanoparticles increases the antioxidant activity quantified as the percentage of DPPH scavenging, as depicted in Fig. 5(E). More than 90% of DPPH-based free radicals were scavenged by the G/CS/TA/AgNP-2 hydrogel formulation, indicating that this formulation can be much more efficient at ROS scavenging in wound conditions than all other fabricated formulations. Also, with an increase in the released amount of the TA from the hydrogels, the DPPH scavenging activity gradually decreased, claiming the concentration-dependent DPPH scavenging activity of the TA.

Antibacterial activity assessment

Furthermore, bacterial infections are a common impediment to wounds. They can postpone curing and increase the possibility of more severe problems by causing inflammation and impairing the body's natural healing processes, leading to tissue damage and necrosis. Preventing bacterial infections at wound sites entails a multi-faceted approach, including the use of antibacterial agents. In this study, the fabricated hydrogels were also loaded with well-known antibacterial agents like TA and AgNPs to tackle bacterial infections at the wound site, and their *in vitro* antibacterial activities against *E. coli* and *S. aureus* are shown in Fig. 5(F)–(K). Initially, the antibacterial activity of the fabricated hydrogels was determined in terms of the percentage of bacterial inhibition using the turbidity method, as demonstrated in Fig. 5(F) and (I). All fabricated hydrogels show *E. coli* and *S. aureus* growth inhibition. Hydrogels G/CS/TA/AgNP-1 and G/CS/TA/AgNP-2 show a significantly higher percentage of bacterial inhibition than all other fabricated hydrogels. This may be due to the synergistic effect of the amalgamation of the AgNPs and TA into the G/CS hydrogel system. G/CS/TA-1, G/CS/TA-AgNP1, G/CS/TA-2, and G/CS/TA-AgNP2 exhibited 78%, 87%, 96%, and 98.2% bacterial inhibition (%) against *E. coli* respectively. Subsequently, G/CS/TA-1, G/CS/TA-AgNP1, G/CS/TA-2, and G/CS/TA-AgNP2 inhibited 72%, 84%, 94%, and 96% of *S. aureus*, respectively. Moreover, the hydrogel's antibacterial activity was also determined using the zone of inhibition method, as demonstrated in Fig. 5(G) and (J). The zones of inhibition created by G/CS/TA-1, G/CS/TA-AgNP1, G/CS/TA-2, and G/CS/TA-AgNP2 against *E. coli* were 5 mm, 6.5 mm, 7 mm, and 9 mm, respectively, as shown in Fig. 5(H). Similarly, against *S. aureus* the zones of inhibition developed by G/CS/TA-1, G/CS/TA-AgNP1, G/CS/TA-2, and G/CS/TA-AgNP2 were 2.9 mm, 5 mm, 6.5 mm, and 8 mm, as shown in Fig. 5(k). Hydrogels depict a better inhibition zone of the *E. coli* bacteria compared to the *S. aureus* bacteria. Among all hydrogels, G/CS/TA/AgNP-2 shows a significantly higher zone of inhibition than all other fabricated hydrogels. The overall antibacterial assessment suggested that the developed G/CS/TA/AgNP-2 hydrogel has competent budding to destroy Gram-positive and Gram-negative types of bacteria whenever they try to grow over the wound site.

In vitro cytotoxicity assay

Evaluating the biological behaviour of fabricated hydrogels is a crucial step for ensuring their safety, efficacy, and suitability in terms of hemocompatibility, cytotoxicity with cells, *in vitro* antioxidant behaviour, antibacterial activity, and *in vivo* response in promoting the complex processes entangled in tissue regeneration and wound healing. First of all, the fabricated hydrogels were initially encountered with blood cells using the hemocompatibility protocol, which is a process of evaluating the compatibility of materials with blood and its components to ensure that the material does not cause any adverse effects on blood and its components, such as clotting, haemolysis, or inflammation (Fig. 6(A)). The fabricated materials will also come in contact with the blood during the application at the wound site. Hence, the blood cell compatibility of the fabricated hydrogels in terms of haemolysis percentage was investigated, as shown in Fig. 6(A) and (B). Fig. 6(A) shows a developed RBC pellet in tubes treated with PBS and all fabricated hydrogels, indicating no significant haemolysis. In contrast, the positive control (Triton-X) illustrates the

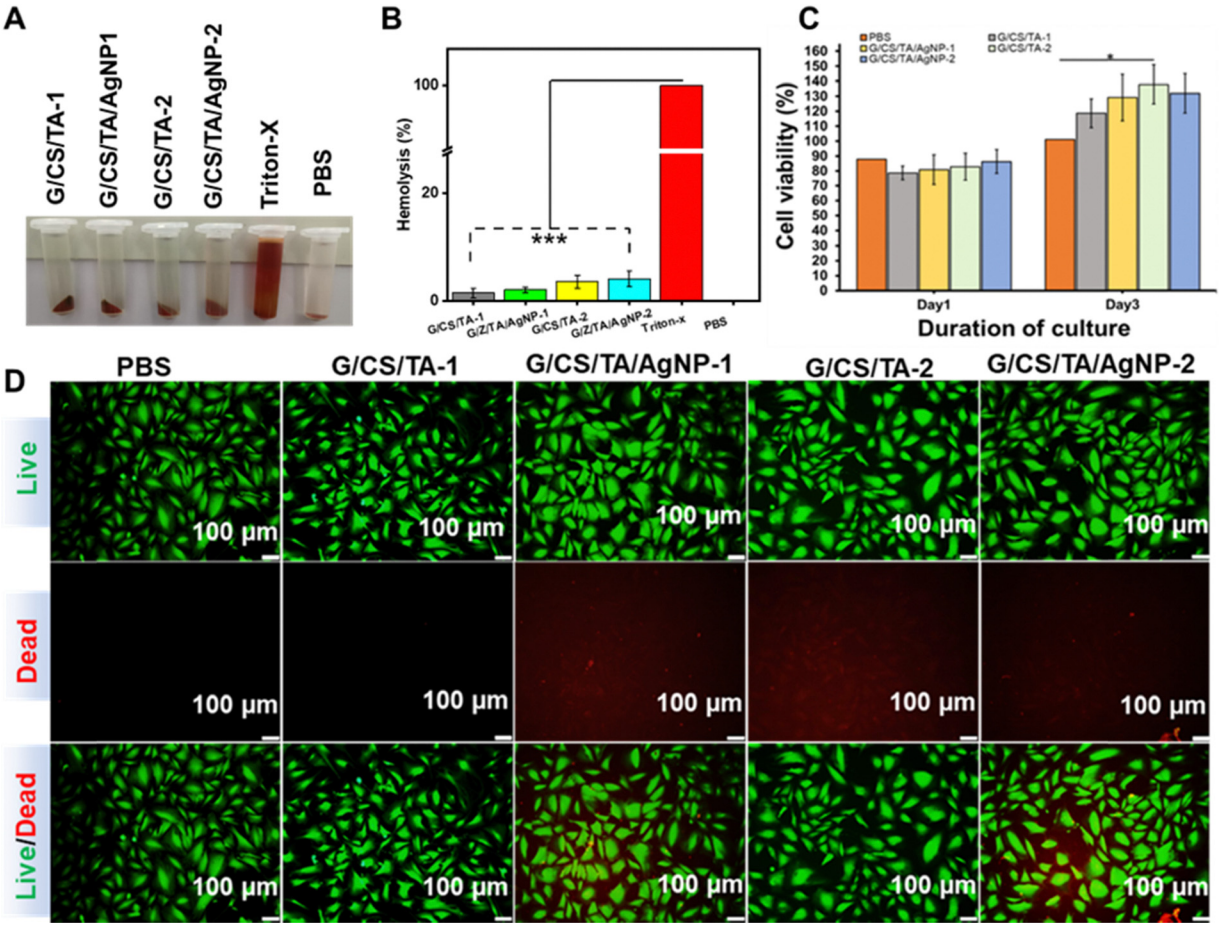

Fig. 6 (A) Biocompatibility of the fabricated hydrogels against the red blood cells (RBC). (B) Percentage of hemolysis by fabricated hydrogels. (C) HDF-n cell viability over the fabricated hydrogels and PBS (control). (D) Live/dead assay with fabricated hydrogel systems. Here, columns and error bars represent mean and standard deviation, whereas $*p < 0.05$, $**p < 0.005$, and $***p < 0.0005$ show the statistical difference.

full-scale haemolysis, as shown by the reddish color of the supernatant. Furthermore, haemolysis was quantified by taking the absorbance of the supernatant (Fig. 6(B)). In Fig. 6(A), quantitative analysis of hemolysis illustrates that G/CS/TA-1, G/CS/TA-AgNP1, G/CS/TA-2, and G/CS/TA-AgNP2 caused 1.44%, 2.00%, 3.55%, and 4.082% hemolysis respectively. All hydrogels show less than 5% of haemolysis. According to the haemolytic index (ASTM standard F756) of implanted materials, all hydrogels should be considered haemocompatible.

Furthermore, cytocompatibility is an essential parameter to check the toxicological behavior of the hydrogel with the fibroblast cells, which will be used for wound healing. Therefore, the cytocompatibility of the fabricated hydrogels was determined by using HDF-n cell lines, as shown in Fig. 6(C). The percentage of cell viability depicts the gradual increase in the HDF-n cell viability (mitochondrial activity) with increasing concentration of the TA and AgNPs in the fabricated G/CS hydrogel systems with increasing time of incubation. The G/CS/TA/AgNP-2 hydrogel was found to be significant compared to the hydrogels G/CS/TA-1 and G/CS/TA-2 and PBS (control). However, some nonsignificant cytotoxic effects of AgNPs and TA were observed, which may be due to the oxidative stress or interaction with the cell membrane. Therefore, it is concluded that incorporating the AgNPs into the fabricated systems is biocompatible with the HDF-n cells, and all hydrogels are also biocompatible.

Moreover, the morphology of seeded HDF-n cells on the fabricated hydrogels was evaluated using a live/dead staining assay, as shown in Fig. 6(D). Histological staining offers diverse insights into cell–biomaterial interactions like cell distribution, cell morphology, and cell spreading. The live stained images show that no significant morphological effect was observed on the cells treated with all hydrogel systems. As early as many researchers have observed, the morphology of all growing cells appears to be healthy.[75] However, slight toxicity was observed as the number of dead cells increased with the concentration of the silver nanoparticles and TA in the composite hydrogels increased, as similarly observed in the MTT assay.

In vivo irregular wound healing activity

The above research outcomes from the various *in vitro* studies well demonstrated that the fabricated hydrogels are tissue adhesive, self-healing, self-adaptable, and easily injectable, show sustained release of tannic acid and AgNPs, and have

antimicrobial properties, favourable antioxidant activity, and biocompatibility with HDF-N fibroblast cells and red blood cells; all these strongly suggest their excellent application potential in irregular deep wound healing. Thus, evaluating the potential of injectable hydrogels for irregular wound healing is crucial for ensuring healing effectiveness, adaptability, and clinical relevance across a spectrum of wound shapes and conditions in real-world applications. For that purpose, the profound full-thickness irregular wound healing potential of the fabricated hydrogels evaluated in a mouse model (Fig. 7(A)) through macroscopic examination of the wound showed significant contraction in the base material group and loaded material group, with an almost healed surface and partial hair regrowth on the 14th day. In Fig. 7(D), it is depicted that the negative control-treated group showed only 92% of wound contraction, whereas the positive control-treated group promoted 98.7% wound contraction. The hydrogel system G/CS/TA/AgNP-2, with silver nanoparticles and TA, showed approximately 100% wound closure and hair growth also, except for a very minor scar remains compared to the control groups. Significant wound closure was also seen in the vehicle group G/CS/TA-2, indicating the effectiveness of the tannic acid used in the formulation (Fig. 7(B)–(D)). The scar tissue formation was greater and more evident in the G/CS/TA-2 and G/CS/TA/AgNP-2 groups as compared to the positive and negative controls. The wound contraction in the G/CS/TA-2 group and the positive control, *i.e.* betadine, was almost similar.

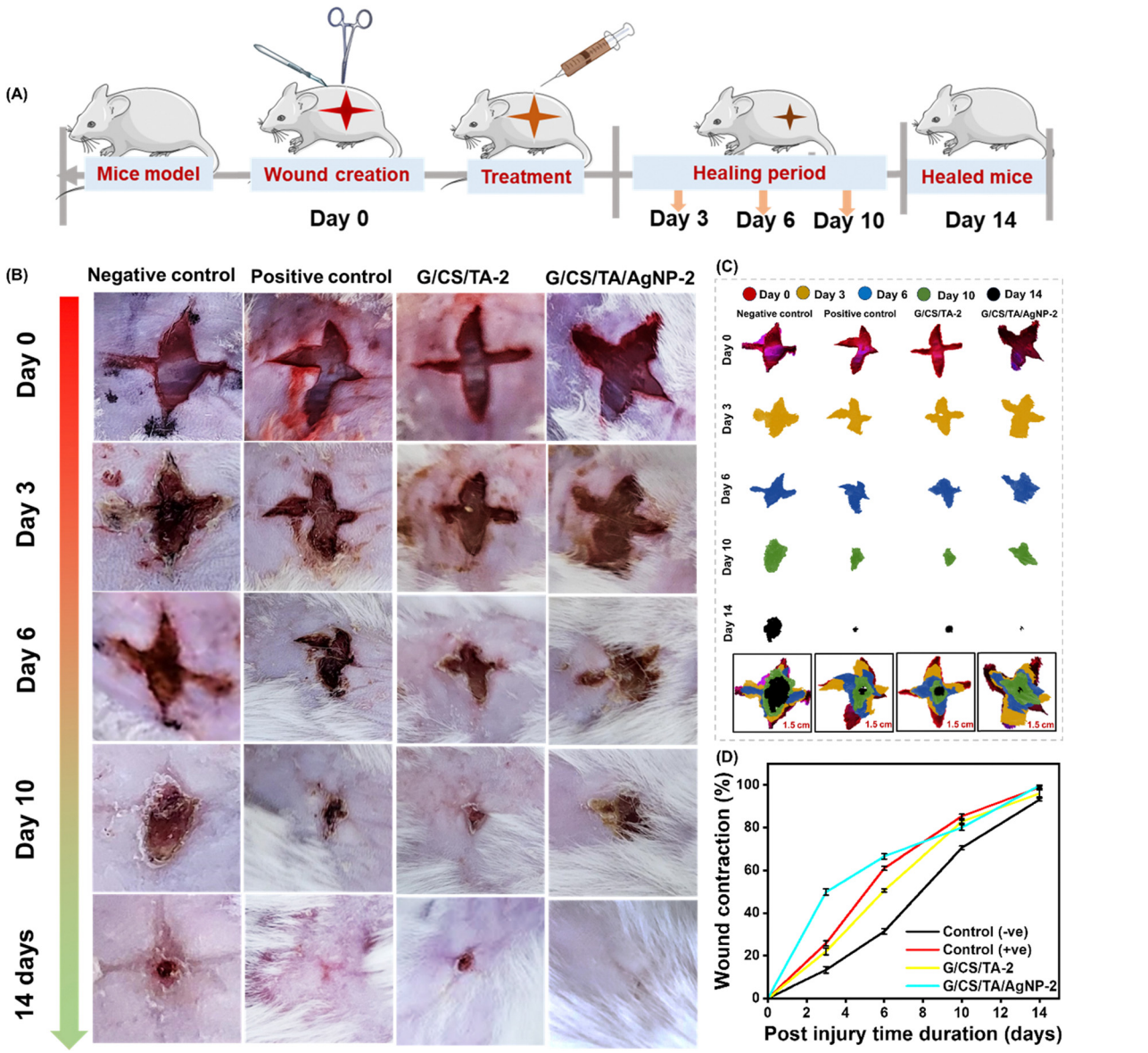

Fig. 7 (A) Schematic of the timeline of the *in vivo* experimental process of the full-thickness irregular wound healing assay. (B) Macroscopic images of the irregular wound closure during 14 days indicating that the silver-loaded hydrogel promotes an increased rate of wound healing in Balb/c mice. (C) Wound healing traces of the different treatment groups. (D) Percentage of the irregular wound contraction over the time period of 14 days. Here, lines and error bars signify the mean and standard deviation.

Furthermore, the histological examination done through the H&E staining method on the healed skin tissues of the mice model also contributed valuable evidence regarding the cellular and tissue level changes that occurred during the wound healing process, demonstrated in Fig. 8(A) and (B). A significant number of fibroblasts were seen in the skin tissues of the group G/CS/TA/AgNP-2 as compared to the negative control group (Fig. 8(A)). Hair follicular formation was highly seen in the skin tissue of G/CS/TA/AgNP-2 treated group on the 14th day, indicating maximum healing. The amount of epidermis was larger in both G/CS/TA-2 and G/CS/TA/AgNP-2 than in the negative control group. Overall, the G/CS/TA/AgNP-2 formulated hydrogel showed a significant difference in the rate of wound healing with a significant decrease in the time taken for

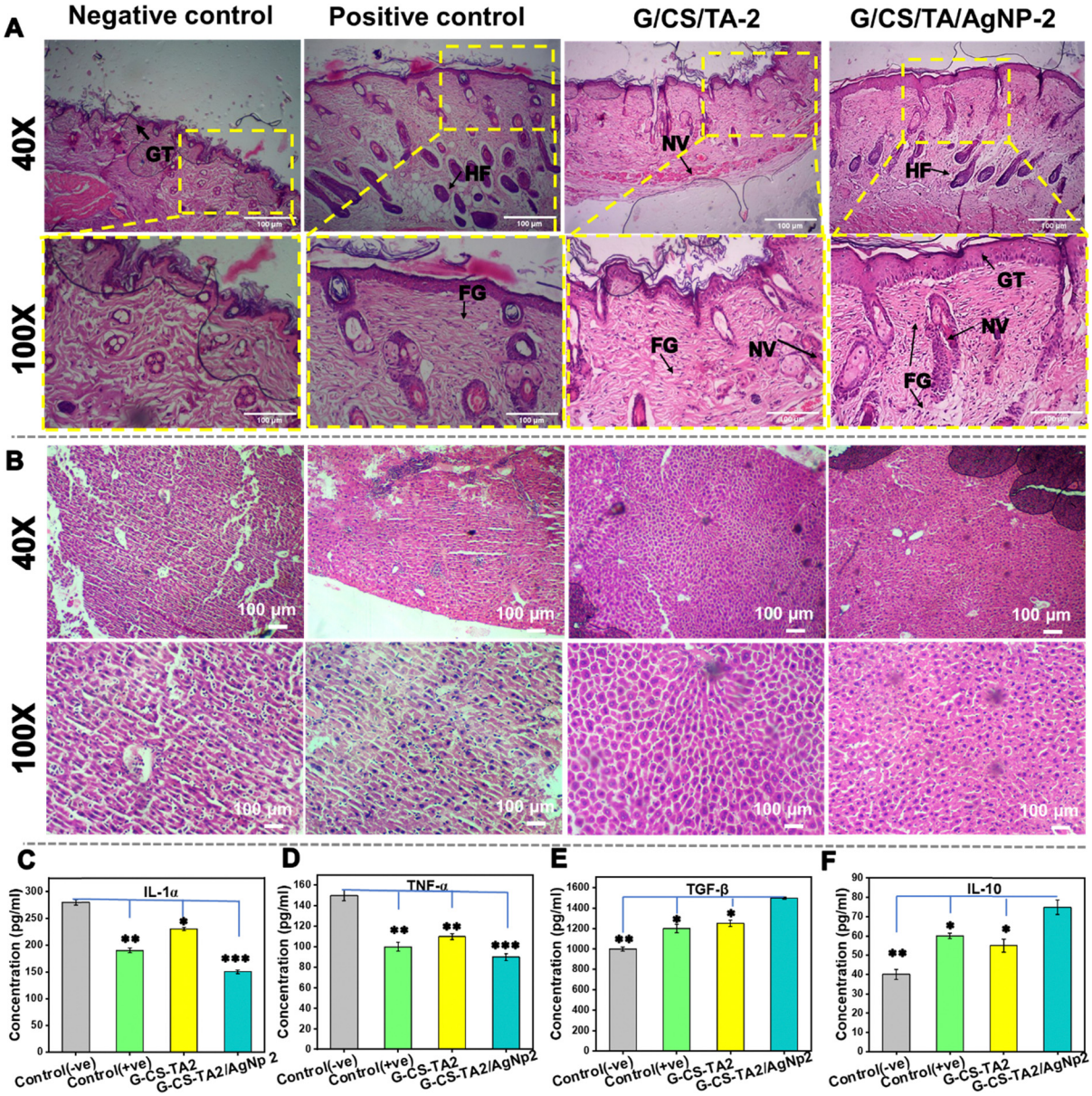

Fig. 8 (A) H&E-stained images of harvested skin sections of the full-thickness irregular wounds on the 14th day as examined at 40× and 100×, indicating various markers of wound healing. HF – hair follicle, GT – granular tissue, NV – neo vasculature, FG – fibroblast growth. (B) H&E-stained images of the liver harvested from the experimental mice on the 14th day as examined at 40× and 100×. Liver histology of all the groups appears to be normal, with normal hepatic lobules that feature central veins and portal tracts. (C) The cytokine graph of IL-1α shows the effect of different topical treatments on the production of cytokine levels on day 14 examined in the Balb/c mouse wound models. (D) Cytokine graph of TNF-α shows the effect of different topical treatments on the production of cytokine levels on day 14 examined in the Balb/c mouse wound models. (E) Cytokine graph of TGF-β shows the effect of different topical treatments on the production of cytokine levels on day 14 examined in the Balb/c mouse wound models. (F) Cytokine graph of IL-10 shows the effect of different topical treatments on the production of cytokine levels on day 14 examined in the Balb/c mouse wound models. Negative control – saline, positive control – commercial betadine. Here, columns and error bars signify mean and standard deviation, whereas * indicates a p value of 0.3.

the irregular wound to heal (Fig. 8(A)). Using gelatin in the formulation has dramatically helped in the proliferation of fibroblasts, and the incorporation of tannic acid has helped the topical formulation adhere to the skin surface. Tannic acid has various supportive bioactive properties, such as antioxidant, anti-inflammatory, and antibacterial, which has also been confirmed by the wound getting healed at a more incredible speed for both G/CS/TA-2 and G/CS/TA/AgNP-2 treated mice groups (Fig. 8(A)). However, the group G/CS/TA/AgNP-2 having silver nano-formulation clearly showed a significant difference in wound closure with the indication of higher wound healing efficacy comparatively. Then again, the negative control group, *i.e.*, the mice subjected to saline treatment, showed incomplete re-epithelialization. The epithelization was more prominent towards the ends as compared to the centre. Observing the tissue histology of the G/CS/TA/AgNP-2 treated group, it shows greater re-epithelialization and structured tissue development. Also, the epidermal thickness of the H&E-stained skin tissue of the different treatment groups was determined. Fig. S5 (ESI†) shows that the epidermal thicknesses of control (−ve), control (+ve), G/CS/TA-2, and the G/CS/TA/AgNP-2 treated mouse groups were 10.56 μm, 26.26 μm, 30.5 μm, and 49.44 μm, respectively. Macrophages and inflammation were evidently visible in the negative control group and, to some extent, the positive control group as well. Moreover, neovascularization is seen effectively in the histology of the loaded material group. The formation of hair follicles is also seen in the tissue histology of the G/CS/TA/AgNP-2 treated group, thus indicating appropriate wound healing. Blue indicates keratinocytes. Hence, it can be concluded that the hydrogel materials containing tannic acid and silver nanoparticles showed significant proliferation and maturation of fibroblasts, leading to expedited wound healing. Moreover, scar tissue formation was greater and more evident in the G/CS/TA-2 and G/CS/TA/AgNP-2 groups than in the positive and negative controls. The wound contraction in the G/CS/TA group and the positive control, *i.e.,* betadine, was almost similar. Moreover, histological examination of liver samples acquired on the 14th day indicated that hepatocytes are intact, retaining their shape and indicating no toxicity of the formulated hydrogels (Fig. 8(B)).

The sandwich-ELISA method, which was performed to quantify various anti-inflammatory and pro-inflammatory cytokines, namely TNF-α, TGF-β, IL-10 and IL-1α, as illustrated in Fig. 8(C)–(F) provided significant insights for the immune responses generated and the anti-inflammatory properties of the formulated hydrogels.[76] TNF-α levels (Fig. 8(D)) of the formulated hydrogel G/CS/TA/AgNP-2 were closer to the positive control group (commercial betadine) and lower than the negative control group (N. saline), showing possibly reduced pro-inflammatory response. TGF-β levels (Fig. 8(E)) were found to be higher in the G/CS/TA/AgNP-2 group than in the G/CS/TA-2 group, indicating higher anti-inflammatory response. IL-1α is a pro-inflammatory cytokine in nature,[77] so its levels in the G/CS/TA/AgNP-2 formulated hydrogel group were significantly lower than those in all other groups, as shown in Fig. 8(C). IL-10 levels in G/CS/TA-2 and G/CS/TA/AgNP-2 hydrogel-treated groups, as seen in Fig. 8(F), show adequate anti-inflammatory response generation. However, further studies need to be done to prove the anti-inflammatory nature of the formulated hydrogel. Overall, the topical application of the G/CS/TA/AgNP-2 hydrogel system turned out to be highly effective in adopting the irregular shape of the wound and accelerating wound healing and an excellent alternative treatment for irregular wounds without using any secondary dressing.

Conclusion

In this study, a dynamically crosslinked injectable bioactive hydrogel was fabricated. The hydrogels were prepared using natural polymers, gelatin, and chondroitin sulfate enriched with *in situ* synthesized AgNPs. $NaBH_4$ was used as a chemical crosslinking and reducing agent of $AgNO_3$ to *in situ* synthesize AgNPs. Tannic acid was used as a physical crosslinker and therapeutic agent. The fabricated hydrogel was porous and adhesive in nature. Hydrogels exhibited self-healing properties due to the presence of reversible borate ester bonds. Hydrogels sustainably released tannic acid and silver nanoparticles. *In vitro* studies demonstrated the biocompatibility, free radical scavenging, and bactericidal activity of the fabricated hydrogels. Furthermore, *in vivo* studies have established the wound healing efficacy of the nanocomposite injectable hydrogel due to the synergistic activity of the tannic acid and AgNPs. ELISA studies also confirmed the anti-inflammatory nature of the hydrogels, mainly due to the presence of tannic acid. Along with these features, the ease of synthesis of the injectable hydrogel makes it a promising candidate as an advanced wound dressing to treat irregular deep skin wounds.

Author contributions

Aniruddha Dan: conceptualization, methodology, software, visualization, data curation, original draft – writing – reviewing and editing; Devanshi Sharma: Conceptualization, visualization, methodology, original draft – writing – reviewing and editing, software and data curation; Hemant Singh: conceptualization, visualization, data curation, methodology, original draft – writing – reviewing and editing; Sunny Kumar: *in vivo* study, original draft – writing and editing; Zeel Bhatia: *in vivo* study, original draft – writing and editing; Sriram Seshadri: resources, validation, reviewing and editing; Shabir Hassan: resources, validation, reviewing and editing; and Mukesh Dhanka: conceptualization, supervision, visualization, investigation, resources, validation, reviewing and editing.

Data availability

The data supporting the findings of this study are available within the article and its ESI† files. Additional data that support the findings of this study, including raw data and detailed experimental protocols, are available from the corresponding author upon reasonable request.

Conflicts of interest

The authors declare that they have no known competing financial interests or personal relationships that could have appeared to influence the work reported in this paper.

Acknowledgements

This study was supported by IP/ITGN/BE/MD/2223/10 and IP/IITGN/BE/MD/2223/13 projects from the Indian Institute of Technology (IIT) Gandhinagar. The authors want to acknowledge the Institute of Science, Ahmedabad, Gujarat, Nirma University, for assisting in the *ex vivo studies* and *in vivo* wound healing studies on mice models. The authors also wish to acknowledge Pandit Deendayal Energy University, Gandhinagar, Gujarat, for the instrumental facility. Furthermore, H. S. and S. H. also acknowledge the Rukshana Mohammed Ali Veettil and Khalifa University of Science and Technology, Abu Dhabi, United Arab Emirates, with Grant No. 8474000442 and 8474000679.

References

1 K. Zheng, Y. Tong, S. Zhang, R. He, L. Xiao, Z. Iqbal, Y. Zhang, J. Gao, L. Zhang, L. Jiang and Y. Li, *Adv. Funct. Mater.*, 2021, **31**(34), 2102599, DOI: **10.1002/adfm.202102599**.
2 Y. Hu, Z. Zhang, Y. Li, X. Ding, D. Li, C. Shen and F. J. Xu, *Macromol. Rapid Commun.*, 2018, **39**(20), 1800069, DOI: **10.1002/marc.201800069**.
3 H. Zhang, X. Sun, J. Wang, Y. Zhang, M. Dong, T. Bu, L. Li, Y. Liu and L. Wang, *Adv. Funct. Mater.*, 2021, **31**(23), 2100093, DOI: **10.1002/adfm.202100093**.
4 H. Grubbs, B. Manna and StatPearls, *Wound physiology*, 2018.
5 R. Laurano, M. Boffito, G. Ciardelli and V. Chiono, *Eng. Regener.*, 2022, **3**, 182–200.
6 J. Li, F. Yu, G. Chen, J. Liu, X. L. Li, B. Cheng, X. M. Mo, C. Chen and J. F. Pan, *ACS Appl. Mater. Interfaces*, 2020, **12**, 2023–2038.
7 M. Wang, J. Du, M. Li, F. Pierini, X. Li, J. Yu and B. Ding, *Biomater. Sci.*, 2023, **11**, 2383.
8 C. M. Leung, C. Dhand, V. Mayandi, R. Ramalingam, F. P. Lim, V. A. Barathi, N. Dwivedi, G. Orive, R. W. Beuerman, S. Ramakrishna, Y. C. Toh, X. J. Loh, N. K. Verma, A. W. C. Chua and R. Lakshminarayanan, *Biomater. Sci.*, 2020, **8**, 3454–3471.
9 Y. Wang, R. Xie, Q. Li, F. Dai, G. Lan, S. Shang and F. Lu, *Biomater. Sci.*, 2020, **8**(7), 1910–1922, DOI: **10.1039/c9bm01635j**.
10 N. Asadi, H. Pazoki-Toroudi, A. R. Del Bakhshayesh, A. Akbarzadeh, S. Davaran and N. Annabi, *Int. J. Biol. Macromol.*, 2021, **170**, 728–750.
11 P. Deng, L. Yao, J. Chen, Z. Tang and J. Zhou, *Carbohydr. Polym.*, 2022, **276**, 118718.
12 H. Weng, W. Jia, M. Li and Z. Chen, *Carbohydr. Polym.*, 2022, **294**, 119767.
13 H. Cui, B. Cui, H. Chen, X. Geng, X. Geng, Z. Li, S. Cao, J. Shen and J. Li, *Biomater. Sci.*, 2023, **11**, 4226.
14 A. Ahmady and N. H. Abu Samah, *Int. J. Pharm.*, 2021, **608**, 121037.
15 I. Lukin, I. Erezuma, L. Maeso, J. Zarate, M. F. Desimone, T. H. Al-Tel, A. Dolatshahi-Pirouz and G. Orive, *Pharmaceutics*, 2022, **14**, 1177.
16 S. P. Ndlovu, K. Ngece, S. Alven and B. A. Aderibigbe, *Polymers*, 2021, **13**, 2959.
17 A. Y. Kim, Y. Kim, S. H. Lee, Y. Yoon, W. H. Kim and O. K. Kweon, *Cell Transplant.*, 2017, **26**, 115–123.
18 M. Zhang, C. Ding, J. Yang, S. Lin, L. Chen and L. Huang, *Carbohydr. Polym.*, 2016, **137**, 410–417.
19 H. Singh, I. Yadav, W. M. Sheikh, A. Dan, Z. Darban, S. A. Shah, N. C. Mishra, S. Shahabuddin, S. Hassan, S. M. Bashir and M. Dhanka, *Int. J. Biol. Macromol.*, 2023, **251**, 126349, DOI: **10.1016/j.ijbiomac.2023.126349**.
20 D. Akın Şahbaz, *Polym. Bull.*, 2024, **81**, 5215–5235.
21 D. Barbieri, R. De Melo Barbosa, P. Severino, E. B. Souto, M. A. De Moraes and C. F. da Silva, *Polymeric Nanosystems: Theranostic Nanosystems*, 2023, vol. 1, pp. 497–520.
22 X. Jiang, Z. Du, X. Zhang, F. Zaman, Z. Song, Y. Guan, T. Yu and Y. Huang, *Front. Bioeng. Biotechnol.*, 2023, **11**, 1158749.
23 F. Mushtaq, A. Raza, S. Rubab Batool, M. Zahid, O. Can Onder, A. Rafique and M. A. Nazeer, *Int. J. Biol. Macromol.*, 2022, **218**, 141–8130.
24 Q. Shen, Y. Guo, K. Wang, C. Zhang and Y. Ma, *Molecules*, 2023, **28**, 7093.
25 R. Sharma, K. Kuche, P. Thakor, V. Bhavana, S. Srivastava, N. K. Mehra and S. Jain, *Carbohydr. Polym.*, 2022, **286**, 119305.
26 T. Mikami and H. Kitagawa, *Biochim. Biophys. Acta, Gen. Subj.*, 2013, **1830**, 4719–4733.
27 W. Wang, L. Shi, Y. Qin and F. Li, *Front. Cell Dev. Biol.*, 2020, **8**, 560442.
28 H. Sodhi and A. Panitch, *Biomolecules*, 2021, **11**, 1–22.
29 A. Rani, R. Baruah and A. Goyal, *Carbohydr. Polym.*, 2017, **159**, 11–19.
30 Y. Zhao, Y. Li, T. Lan, B. Wang, M. Huang, H. Huang, C. Qiao and J. Sun, *Gels*, 2022, **8**, 620.
31 X. Zhang, Z. Ma, Y. Ke, Y. Xia, X. Xu, J. Liu, Y. Gong, Q. Shi and J. Yin, *Mater. Adv.*, 2021, **2**, 5150–5159.
32 H. Rong, Y. Dong, J. Zhao, X. Zhang, S. Li, Y. Sun, T. Lu, S. Yu and H. Hu, *Int. J. Biol. Macromol.*, 2023, **248**, 125739.
33 F. Masood, M. A. Makhdoom, I. A. Channa, S. J. Gilani, A. Khan, R. Hussain, S. A. Batool, K. Konain, S. U. Rahman, A. Wadood, M. N. bin Jumah and M. A. U. Rehman, *Gels*, 2022, **8**, 676.
34 S. A. Shah, M. Sohail, S. A. Khan and M. Kousar, *Mater. Sci. Eng., C*, 2021, **126**, 112169.
35 C. Y. Ewald, *Front. Aging*, 2021, **2**, 741843.
36 G. Wu, F. Ma, Y. Xue, Y. Peng, L. Hu, X. Kang, Q. Sun, D. F. Ouyang, B. Tang and L. Lin, *Carbohydr. Polym.*, 2022, **278**, 118996, DOI: **10.1016/j.carbpol.2021.118996**.
37 L. Zhou, L. Fan, F. M. Zhang, Y. Jiang, M. Cai, C. Dai, Y. A. Luo, L. J. Tu, Z. N. Zhou, X. J. Li, C. Y. Ning, K. Zheng, A. R. Boccaccini and G. X. Tan, *Bioact. Mater.*, 2021, **6**, 890–904.
38 X. Li, Q. Xu, M. Johnson, X. Wang, J. Lyu, Y. Li, S. McMahon, U. Greiser and W. Wang, *Biomater. Sci.*, 2021, **9**, 4139.

39 M. Mihajlovic, M. Rikkers, M. Mihajlovic, M. Viola, G. Schuiringa, B. C. Ilochonwu, R. Masereeuw, L. Vonk, J. Malda, K. Ito and T. Vermonden, *Biomacromolecules*, 2022, **23**, 1350–1365.
40 R. R. Kudarha and K. K. Sawant, *Drug Delivery Transl. Res.*, 2021, **11**, 1994–2008.
41 P. Darvin, Y. H. Joung, D. Y. Kang, N. Sp, H. J. Byun, T. S. Hwang, H. Sasidharakurup, C. H. Lee, K. H. Cho, K. Do Park, H. K. Lee and Y. M. Yang, *J. Cell. Mol. Med.*, 2017, **21**, 720–734.
42 C. Chen, H. Yang, X. Yang and Q. Ma, *RSC Adv.*, 2022, **12**, 7689–7711.
43 M. Ghasemian, F. Kazeminava, A. Naseri, S. Mohebzadeh, M. Abbaszadeh, H. S. Kafil and Z. Ahmadian, *Biomed. Pharmacother.*, 2023, **166**, 115328.
44 T. Park, W. Il Kim, B. J. Kim, H. Lee, I. S. Choi, J. H. Park and W. K. Cho, *Langmuir*, 2018, **34**, 12318–12323.
45 H. Jafari, P. Ghaffari-Bohlouli, S. V. Niknezhad, A. Abedi, Z. Izadifar, R. Mohammadinejad, R. S. Varma and A. Shavandi, *J. Mater. Chem. B*, 2022, **10**, 5873–5912, DOI: **10.1039/d2tb01056a**preprint.
46 C. Chen, H. Yang, X. Yang and Q. Ma, *RSC Adv.*, 2022, **12**, 7689–7711, DOI: **10.1039/d1ra07657d**preprint.
47 K. Fang, Q. Gu, M. Zeng, Z. Huang, H. Qiu, J. Miao, Y. Fang, Y. Zhao, Y. Xiao, T. Xu, R. P. Golodok, V. V. Savich, A. P. Ilyushchenko, F. Ai, D. Liu and R. Wang, *J. Mater. Chem. B*, 2022, **10**, 4142–4152.
48 W. Pan, X. Qi, Y. Xiang, S. You, E. Cai, T. Gao, X. Tong, R. Hu, J. Shen and H. Deng, *Int. J. Biol. Macromol.*, 2022, **195**, 190–197.
49 M. Cheng, L. Hu, G. Xu, P. Pan, Q. Liu, Z. Zhang, Z. He, C. Wang, M. Liu, L. Chen and J. Chen, *Colloids Surf., B*, 2023, **227**, 113354, DOI: **10.1016/j.colsurfb.2023.113354**.
50 C. Chen, X. W. Geng, Y. H. Pan, Y. N. Ma, Y. X. Ma, S. Z. Gao and X. J. Huang, *RSC Adv.*, 2020, **10**, 1724–1732.
51 A. Rafiq, S. Tehseen, T. A. Khan, M. Awais, A. R. Sodhozai, C. H. Javed, M. F. Ullah, N. Ali, M. Y. Alshahrani, M. I. Khan and A. M. Galal, *Biomass Convers. Biorefin.*, 2023, **13**(17), 15531–15541, DOI: **10.1007/s13399-022-02960-w**.
52 A. Taglietti, C. R. Arciola, A. D'Agostino, G. Dacarro, L. Montanaro, D. Campoccia, L. Cucca, M. Vercellino, A. Poggi, P. Pallavicini and L. Visai, *Biomaterials*, 2014, **35**, 1779–1788.
53 S. Dutt Purohit, H. Singh, R. Bhaskar, I. Yadav, C.-F. Chou, M. Kumar Gupta and N. Chandra Mishra, *Mater. Sci. Eng., C*, 2020, **116**, 111111, DOI: **10.1016/j.msec.2020.111111**.
54 H. Singh, A. Dan, B. Prasanna Kumari, H. Dave, N. Parsaila, A. Navale, Z. Darban, I. Yadav, P. Goyal, S. K. Misra, S. Shahabuddin, S. Hassan and M. Dhanka, *Biomater. Adv.*, 2024, **164**, 213983, DOI: **10.1016/j.bioadv.2024.213983**.
55 S. Dutt Purohit, R. Bhaskar, H. Singh, I. Yadav, M. Kumar Gupta and N. Chandra Mishra, *Int. J. Biol. Macromol.*, 2019, **133**, 592–602, DOI: **10.1016/j.ijbiomac.2019.04.113**.
56 H. Singh, S. Hassan, S. U. Nabi, N. C. Mishra, M. Dhanka, S. D. Purohit, N. A. Ganai, R. Bhaskar, S. S. Han, A. U. H. Qurashi and S. M. Bashir, *Int. J. Biol. Macromol.*, 2024, **255**, 127810.
57 C. D. F. Moreira, S. M. Carvalho, R. G. Sousa, H. S. Mansur and M. M. Pereira, *Mater. Chem. Phys.*, 2018, **218**, 304–316.
58 H. Vithalani, H. Dave, H. Singh, D. Sharma, A. Navale and M. Dhanka, *Biomater. Adv.*, 2025, **169**, 214195.
59 H. Dave, H. Vithalani, H. Singh, I. Yadav, A. Jain, A. Pal, N. Patidar, A. Navale and M. Dhanka, *Small*, 2025, **21**, 2405508.
60 Y. Zheng, Y. Liang, D. Zhang, X. Sun, L. Liang, J. Li and Y. N. Liu, *ACS Omega*, 2018, **3**, 4766–4775.
61 U. B. Demirci and P. Miele, *C. R. Chim*, 2014, **17**, 707–716.
62 L. Dai, B. Nadeau, X. An, D. Cheng, Z. Long and Y. Ni, *Sci. Rep.*, 2016, **6**, 36497, DOI: **10.1038/srep36497**.
63 R. Deka, S. Sarma, P. Patar, P. Gogoi and J. K. Sarmah, *Carbohydr. Polym.*, 2020, **248**, 116786.
64 H. Ullah, S. Qamar, F. Khan, F. Raheem, A. Shamim, I. Uddin, Z. Ur Rehman, F. Ahmad and M. R. Shah, *J. Ongoing Chem. Res.*, 2019, **4**(1), 24–31, DOI: **10.5281/zenodo.3561139**.
65 T. T. Le, C. Pistidda, J. Puszkiel, C. Milanese, S. Garroni, T. Emmler, G. Capurso, G. Gizer, T. Klassen and M. Dornheim, *Metals*, 2019, **9**(10), 1061, DOI: **10.3390/met9101061**.
66 B. Ari, M. Sahiner, S. Demirci and N. Sahiner, *Polymers*, 2022, **14**(1), 70, DOI: **10.3390/polym14010070**.
67 X. Feng, X. Hou, C. Cui, S. Sun, S. Sadik, S. Wu and F. Zhou, *Eng. Regener.*, 2021, **2**, 57–62.
68 H. Jafari, P. Ghaffari-bohlouli, D. Podstawczyk, L. Nie and A. Shavandi, *Carbohydr. Polym.*, 2022, **295**, 119844.
69 H. Fan, J. Wang, Q. Zhang and Z. Jin, *ACS Omega*, 2017, **2**, 6668–6676.
70 H. Fan, J. Wang and Z. Jin, *Macromolecules*, 2018, **51**, 1696–1705.
71 Y. Yang, X. Zhao, S. Wang, Y. Zhang, A. Yang, Y. Cheng and X. Chen, *Nat. Commun.*, 2023, **14**, 1–14.
72 W. S. Al-Arjan, M. U. A. Khan, H. H. Almutairi, S. M. Alharbi and S. I. A. Razak, *Polymers*, 2022, **14**(10), 1949, DOI: **10.3390/polym14101949**.
73 F. A. Agili and S. F. M. Aly, *Polym. Polym. Compos.*, 2020, **28**, 598–608.
74 M. Saidi, A. Dabbaghi and S. Rahmani, *Polym. Bull.*, 2020, **77**, 3989–4010.
75 C. Chittasupho, A. Manthaisong, S. Okonogi, S. Tadtong and W. Samee, *Int. J. Mol. Sci.*, 2021, **23**(1), 142, DOI: **10.3390/ijms23010142**.
76 J. Y. Chen, H. Wu, H. Li, S. L. Hu, M. M. Dai and J. Chen, *Int. Immunopharmacol.*, 2015, **24**, 102–109.
77 D. Zhou, T. Liu, S. Wang, W. He, W. Qian and G. Luo, *Front. Physiol.*, 2020, **11**, 5450, DOI: **10.3389/fphys.2020.545008**.

